Acoustical modeling and Bayesian inference for rigid porous media in the low-mid frequency regime

Remi Roncen, Zine E.A. Fellah, Denis Lafarge, Estelle Piot, Frank Simon, Erick Ogam, Mohamed Fellah, Claude Depollier

Acoustical Modeling and Bayesian Inference for Rigid Porous Media in the Low-Mid Frequency Regime

R. Roncen [*1], Z.E.A. Fellah[2], D. Lafarge[3], E. Piot[1], F. Simon[1], E. Ogam[2], M. Fellah[4] and C. Depollier [†5]

[1]ONERA / DMPE, Université de Toulouse, F-31055, Toulouse, France
[2]LMA, CNRS, UMR 7031, Aix-Marseille Univ, Centrale Marseille, F-13402 Marseille Cedex 20, France
[3]LUNAM Universite du Maine, UMR CNRS 6613 Laboratoire d'Acoustique de l'Universite du Maine UFR STS Avenue O. Messiaen 72085 Le Mans CEDEX 09, France
[4]Laboratoire de Physique Théorique, Faculté de Physique, USTHB, BP 32 El Alia, Bab Ezzouar 16111, Algeria
[5]MPEI, Krasnokazarmennaya 14 Moscow 111250, Russia

Abstract

In this paper, a modeling extension for the description of wave propagation in porous media at low-mid frequencies is introduced. To better characterize the viscous and inertial interactions between the fluid and the structure in this regime, two additional terms described by two parameters α_1 and α_2 are taken into account in the representation of the dynamic tortuosity in a Laurent-series on frequency. The model limitations are discussed. A sensitivity analysis is performed, showing that the influence of α_1 and α_2 on the acoustic response of porous media is significant. A general Bayesian inference is then conducted to infer simultaneously the posterior probability densities of the model parameters. The proposed method is based on the measurement of waves transmitted by a slab of rigid porous material, using a temporal model for the direct and inverse transmission problem. Bayesian inference results obtained on three different porous materials are presented, which suggest that the two additional parameters are accessible and help reducing systematic errors in the identification of other parameters: porosity, static viscous permeability, static viscous tortuosity, static thermal permeability and static thermal tortuosity.

I Introduction

Porous media are of great interest for a wide range of applications: noise control [1], hydrology [2], biology [3], etc. Wave propagation in air-saturated porous materials is determined by the viscous, inertial and thermal interactions between the fluid and solid phases, which can usually be modeled assuming divergence-free fluid motion at the pore scale. Depending on the frequency range considered, the physical intrinsic parameters describing the porous material acoustic behavior are distinct. In the high-frequency regime, where the fluid flow can be considered inviscid adiabatic in the bulk fluid except for a lossy boundary layer at the pore walls, the inertial effects and the viscous and thermal dissipative effects are mainly characterized by the tortuosity α_∞ and the viscous and thermal characteristic lengths of the pores [4, 1] (Λ and Λ', respectively). In the low-frequency regime, where the fluid flow can be considered viscous isothermal within the pores, the viscous and inertial effects are mainly described by the static viscous permeability k_0 and the static viscous tortuosity

*Corresponding author: remi.roncen@onera.fr
†Also at: LUNAM Universite du Maine, UMR CNRS 6613 Laboratoire d'Acoustique de l'Universite du Maine UFR STS Avenue O. Messiaen 72085 Le Mans CEDEX 09, France

α_0 (also coined inertial factor [5, 6]). The thermal effects are described by the static thermal permeability k'_0 [6, 7] and the static thermal tortuosity α'_0 [6, 1]. In this regime we will see however that if we consider the effect of the two last thermal parameters, we should simultaneously consider the effect of two more, higher order, viscous and inertial parameters. The porosity ϕ influences both asymptotic regimes. The modeling of wave propagation inside porous media and the non invasive determination of their micro-structure are crucial for the diverse research fields in which porous materials are studied, sparking a vast interest in their characterization.

Dedicated direct measurements have been performed in order to individually access some of these parameters [8, 9, 10, 11], but some drawbacks (intrusive measurements, specialized equipment, need of different samples for each experiment) have oriented the identification strategies towards new characterization methods. Auspiciously, all the morphological characteristics of a porous material have a certain influence on its acoustical response, which has naturally led to the development of acoustical indirect identification methods that allow the inference of these properties from acoustic measurements (see [12] for a review on these methods and [13] for an application in outdoor ground characterization). The general idea of such an inverse identification is to fit the output of an acoustic model to a measurement. Inverse characterization methods are preferred, since they allow the simultaneous identification of multiple parameters, while using prevailing equipment such as wave guides (impedance tube, transmission tube) or ultrasonic transducers.

In [14, 15], the static viscous permeability k_0 was successfully identified using transmitted and reflected waves of very low-frequency bandwidth, in the time domain. In [16], the direct problem of wave propagation in air-saturated porous media was worked out at low frequencies, using the inertial parameter of Norris α_0 in the low frequency approximation of the tortuosity. This model was later used in [17], where an inverse scattering problem was solved in the time domain to obtain both the static thermal permeability k'_0 and the static viscous tortuosity α_0 simultaneously, using transmitted waves in the low-frequency range. Based on measurements of the surface impedance of a porous sample backed by different air gaps, the method developed by Zieliński [18] allowed the simultaneous retrieval of the 6 parameters of the Johnson–Champoux–Allard–Lafarge [4, 19, 7] JCAL model (ϕ, α_∞, k_0, Λ, Λ' and k'_0), using impedance tube experiments, in the frequency domain.

While the studies conducted on the inverse identification of porous material properties presented hereinbefore focused on a deterministic fit between models and experiments, and were thus exempt from any statistical analysis of the inversion outcome, Chazot et al. [20] pioneered a Bayesian inference approach for this kind of identification, taking into account measurement uncertainties in the inversion and using a transmission tube to obtain pressure measurements in the audio-frequency regime on both sides of a clamped poroelastic material. The inference of ϕ, α_∞, k_0, Λ and Λ' (plus 3 parameters of the Biot model) was conducted using a Differential-Evolution Markov-Chain Monte-Carlo strategy to explore the marginal posterior probability of each parameters. Later, Niskanen et al. [21] conducted both deterministic and statistical inversions on porous samples in the frequency domain, in a Bayesian setting similar to the one in [20], using measurements in an impedance tube and a transmission tube. Their work showed the ability of Bayesian inference methods to efficiently invert the JCAL parameters and the associated uncertainties. More recently, Bayesian inference was used [22] to carry the identification of ϕ, α_∞, Λ and Λ' using ultrasonic reflected waves by the first interface, in the time dimain.

Extensions of the Johnson–Champoux–Allard (JCA [4, 19]) equivalent fluid model were proposed by Norris [5] and Lafarge [6, 23] to correct the low frequency behavior of visco-inertial and thermal effects. However, the more detailed full-frequency model proposed so far, the JCAPL (Johnson–Champoux–Allard–Pride–Lafarge) model [6, 1, 23] turns out to be inappropriate to describe precisely the low-mid frequency range. Indeed, JCAPL uses the same number of low-frequency viscous, inertial and thermal parameters. But the effective density, in accordance with its Laurent series which starts at a power $(\mathrm{j}\omega)^{-1}$, will require two additional parameters to be described with the same precision as the effective compressibility (which starts at a power

$(\mathrm{j}\omega)^0$ with a pure physical constant γ). Therefore, a consistent description of the low-mid frequencies visco-inertial effects should introduce $N+2$ geometrical parameters, N being the number used for thermal effects. The current modeling of visco-inertial effects should be extended by introducing two additional parameters, due to the strong influence of visco-inertial effects on porous media acoustics at low-mid frequencies. In particular, these parameters should be able to represent the deviation from the purely viscous regime, when inertial effects start growing within the intra-pore fluid-flow.

The purpose of the present work is thus twofold. The main goal is to extend the previous equivalent fluid model in the low-mid frequency range, with the introduction of the two new parameters, and to understand their influence on the acoustic behavior of porous media. The second objective set in the present study is to evaluate the model parameters using a Bayesian inference method in a setting similar to the one in [20, 21], but using measurements of transmitted waves in the time domain. The attractive feature of a time-domain-based approach is that the analysis is naturally limited by the signals finite duration, and is consequently the most appropriate approach to transient signal processing. To perform the identification of the new higher order parameters, all the other parameters are also identified simultaneously, including the inertial parameter of Norris, which has not been done before.

This paper is organized as follows. The acoustical model is presented in Sec. II, where the new intrinsic parameters are detailed, and their influence on the acoustic response highlighted. The inference methodology is described in Sec. III, where the Bayes formula is recalled and the numerical exploration of the parameter space is detailed. Results for the inference of three different porous materials are presented in Sec. IV. Concluding remarks are laid out in Sec. V.

II Acoustical Modeling

In the study of porous media, two different cases typically arise. When the fluid and solid phases have coupled contributions to the acoustic attenuation in the material, the Biot model is used to describe the wave propagation in both the solid and fluid phases [24], resulting in the occurrence of two compressional and one rotational wave. When the solid structure can be assumed rigid and its vibrations neglected, which is often the case in air-saturated porous media, one usually resorts to using an equivalent fluid model where only the compressional wave propagation in the fluid phase of the porous material is considered. The classical properties of density and compressibility are replaced by equivalent ones in order to take into account visco-inertial and thermal fluid-structure interactions in the pores.

A Extension of the acoustical low frequency modeling for rigid porous media

Let us consider a macroscopically homogeneous rigid porous material filled with a fluid of density ρ_f, fluid adiabatic bulk modulus K_f and dynamic viscosity η. We further assume that the geometry is simple enough so that the movement of the fluid remains incompressible at the pore scale. One can then apply continuum mechanics to the fluid phase in the material and identify the whole porous medium as an equivalent fluid material of effective properties to account for viscous and thermal dissipation arising from the fluid-frame interaction. As initially proposed by Zwikker and Kosten [25], one can decouple the contribution of viscous and thermal dissipation in the pores. To do so, one defines two response factors that represent the deviation from fluid behavior in free space as a function of frequency: the dynamic tortuosity $\alpha(\omega)$ that encompasses all viscous and inertial effects, and the dynamic compressibility $\beta(\omega)$ that takes into account all thermal effects. In the time domain, these factors are operators [26] (with kernels $\tilde{\alpha}(t)$, $\tilde{\beta}(t)$) and the equations controlling the wave behavior are given by

$$\rho_f \int_0^t \tilde{\alpha}(t-\tau)\frac{\partial \boldsymbol{v}(\tau)}{\partial \tau}\mathrm{d}\tau = -\nabla p, \quad \frac{1}{K_f}\int_0^t \tilde{\beta}(t-\tau)\frac{\partial p(\tau)}{\partial \tau}\mathrm{d}\tau = -\nabla\cdot\boldsymbol{v}. \tag{1}$$

In the previous equations, $\boldsymbol{v}$ is the macroscopic fluid velocity and p the acoustic pressure, obtained by averaging the microscopic velocity and pressure fields over a representative elementary volume. The integration limits t and 0 respectively account for causality and absence of motion for $t < 0$.

In this study, we propose to enhance the modeling of $\alpha(\omega)$ in the low-mid frequency range (so that the viscous boundary layer thickness $\delta = (2\eta/\omega\rho_f)^{1/2}$ is larger than the typical radius r of the pores), by taking into account two more terms in its Laurent series expansion (as compared with the work of Norris [5] and the JCAPL model [23]). This reads, in the frequency domain, as

$$\alpha(\omega) = \frac{\omega_v}{\mathrm{j}\omega} + \alpha_0 - \alpha_1^2 \left(\frac{\mathrm{j}\omega}{\omega_v}\right) + \alpha_2^3 \left(\frac{\mathrm{j}\omega}{\omega_v}\right)^2 + \mathcal{O}\left(\frac{\mathrm{j}\omega}{\omega_v}\right)^3, \tag{2}$$

with $\mathrm{j}^2 = -1$, $+\mathrm{j}\omega$ is the time derivative, $\omega_v = \eta\phi/(\rho_f k_0)$ is a frequency characteristic of the viscous effects, ϕ is the porosity, k_0 is the static viscous permeability and α_0 is the static viscous tortuosity. α_1 and α_2 are two new positive dimensionless intrinsic geometrical parameters related to the low frequency dynamics of the viscous-inertial forces between fluid and structure, to be discussed in the remainder of this work. The signs associated with the additional terms stem from a physical analysis, given in Sec. B.
The dynamic thermal compressibility is given by [23]

$$\beta(\omega) = \gamma - (\gamma - 1)/\alpha'(\omega), \tag{3}$$

where the dynamic thermal tortuosity $\alpha'(\omega)$ is

$$\alpha'(\omega) = \frac{\omega_\tau}{\mathrm{j}\omega} + \alpha_0' + \mathcal{O}\left(\frac{\mathrm{j}\omega}{\omega_\tau}\right), \tag{4}$$

with $\omega_\tau = \eta\phi/(\rho_f k_0' \mathrm{Pr})$ a frequency characteristic of the thermal effects, where k_0' is the static thermal permeability, α_0' is the static thermal tortuosity, γ is the fluid heat capacity ratio and Pr is the Prandtl number. Note that the dynamic thermal tortuosity Laurent series in 4 is limited to its first two terms since it yields, inserted in 3, a $\beta(\omega)$ expansion up to terms of order $(\mathrm{j}\omega)^2$, the same as in 2:

$$\beta(\omega) = \gamma - (\gamma - 1)\left[\frac{\mathrm{j}\omega}{\omega_\tau} + \alpha_0'\left(\frac{\mathrm{j}\omega}{\omega_\tau}\right)^2\right] + \mathcal{O}\left(\frac{\mathrm{j}\omega}{\omega_\tau}\right)^3. \tag{5}$$

Therefore, α_1' and α_2', the thermal counterparts of visco-inertial parameters α_1 and α_2, need not be considered here.

B Physical interpretation of α_0, α_1, α_2, α_0'

The focus in this study is put on the visco-inertial terms intervening in the modeling of $\alpha(\omega)$. Their physical interpretation is given in the following.

- ▷ The static viscous tortuosity α_0 (also coined inertial factor [5]) corresponds to the real part of the low frequency limit of the dynamic tortuosity, given by Norris [5] and Lafarge [6]: $\alpha_0 = \langle v^2(\boldsymbol{r})\rangle / \langle v(\boldsymbol{r})\rangle^2$ (seel also [23]), where $\langle v(\boldsymbol{r})\rangle$ is the average velocity of the viscous fluid for direct current flow within a volume element, small compared with the relevant wavelength but large compared with the individual material pores. It represents a measure of the direct current viscous-flow disorder, and is increased by irregular solid distributions or by constrictions within the pores [23]. The inertial factor is indirectly related to the standard deviation of the pore size distribution [12], with increasing values when the standard deviation increases. For cylindrical circular pores with log-normally distributed radius of

standard deviation σ_R, the inertial factor is [12] $\alpha_0 = \frac{4}{3}\alpha_\infty e^{4(\sigma_R \ln 2)^2}$. This parameter has been used before to determine the acoustic properties of multi-periodic composites [27], but experimental techniques to measure it are very scarce in the literature [17]. The thermal counterpart of α_0, the thermal tortuosity α_0', is similarly defined [6, 23] by $\alpha_0' = \left\langle \theta^2(\boldsymbol{r}) \right\rangle / \left\langle \theta(\boldsymbol{r}) \right\rangle^2$, where $\langle \theta(\boldsymbol{r}) \rangle$ is the average of the relaxed excess temperature field. This parameter has not been measured experimentally before.

▷ The dimensionless parameter α_1 is related to the low-frequency dynamics of the viscous forces between fluid and structure. The dimensionless parameter α_2 is related to the low-frequency dynamics of the inertial forces between fluid and structure. We can rewrite Eq. 2 in terms of an apparent characteristic frequency $\omega_{c\,\mathrm{app}}$ and an apparent inertial factor $\alpha_{0\,\mathrm{app}}(\omega)$ as

$$\alpha(\omega) = \frac{\omega_{c\,\mathrm{app}}(\omega)}{\mathrm{j}\omega} + \alpha_{0\,\mathrm{app}}(\omega), \tag{6}$$

with

$$\omega_{c\,\mathrm{app}}(\omega) = \frac{\eta\phi}{\rho_f k_{0\,\mathrm{app}}(\omega)}, \tag{7}$$

which introduces $k_{0\,\mathrm{app}}(\omega)$, an apparent permeability function. From the expressions 6,7 and the expansion 2, we find for the apparent permeability function

$$k_{0\,\mathrm{app}}(\omega) = k_0 \left(\frac{1}{1 - \alpha_1^2 \left(\frac{\mathrm{j}\omega}{\omega_v} \right)^2 + \mathcal{O}\left(\mathrm{j}\omega\right)^4} \right), \tag{8}$$

and for the apparent inertial factor $\alpha_{0\,\mathrm{app}}(\omega)$

$$\alpha_{0\,\mathrm{app}}(\omega) = \alpha_0 + \alpha_2^3 \left(\frac{\mathrm{j}\omega}{\omega_v} \right)^2 + \mathcal{O}\left(\mathrm{j}\omega\right)^4. \tag{9}$$

We can now justify a posteriori the signs associated with α_1^2 and α_2^3 in Eq. 2. It suffices to invoke the general property that, because of the divergence-free nature of the fluid flow, the functions $k_{0\,\mathrm{app}}(\omega)$ and $\alpha_{0\,\mathrm{app}}(\omega)$ necessarily are strictly decreasing functions of frequency: $\frac{\mathrm{d}}{\mathrm{d}\omega} k_{0\,\mathrm{app}}(\omega) < 0$ and $\frac{\mathrm{d}}{\mathrm{d}\omega} \alpha_{0\,\mathrm{app}}(\omega) < 0$. Indeed, these are the inequalities (18) in Ref. [28], where the theory of asymptotic homogenization at two scales was used to derive the condition of incompressibility. We consider it more lucid to recognize in this condition a mere hypothesis that is made on the microgeometries considered, then making the detour by the homogenization method in question useless. In fact, as we assume that the pore geometry is simple enough to ensure that the fluid motion is incompressible at the pore scale for large wavelengths, it follows that in the Laplace space the dynamic tortuosity and permeability, $\alpha(s)$ and $k(s)$, are positive strictly decreasing functions of the Laplace variable $s > 0$. In Fourier space the consequence is the same as the one seen above. Monotonic properties of this type, induced by the incompressibility, were also shown in Ref. [6]. Interpretations in terms of economy-of-nature conditions, as mentioned by Brown [29], can also be given. For instance, the fact that $k_{0\,\mathrm{app}}(\omega)$ is maximum at zero frequency interprets as a principle of minimum dissipation, requiring that the direct current flow is that which minimizes the dissipation induced by internal friction. Put another way, the viscous resistance due to the fluid flowing through the pores is minimized, or alternatively, the permeability is made maximum. The velocity profiles of the viscous fluid in permanent regime are distributed in such a way that the ratio $\left\langle \boldsymbol{v}^2 \right\rangle / \left(- \left\langle \boldsymbol{v} \cdot \Delta\boldsymbol{v} \right\rangle \right)$ is made maximum. For the apparent permeability defined in Eq. 8 (which can be shown to be $\left\langle \boldsymbol{v} \cdot \boldsymbol{v}^* \right\rangle / \left(- \left\langle \boldsymbol{v} \cdot \Delta\boldsymbol{v}^* \right\rangle \right)$, see [30, 6]), this means that its value must be maximum at zero frequency, which leads to the minus sign in front of α_1^2. As the apparent permeability decreases as the frequency increases, the porous material becomes, in appearance, more resistive.

Likewise, the fact that $\alpha_{0\,\mathrm{app}}(\omega)$ is maximum at zero frequency interprets as a principle of added mass

maximization: the velocity profiles of the viscous fluid in permanent regime are distributed in such a way that the ratio $\langle \boldsymbol{v}^2 \rangle / \langle \boldsymbol{v} \rangle^2$ is made maximum. For the dynamic tortuosity defined in Eqs.(6–7) (which can be shown [30, 6] to be $\langle \boldsymbol{v} \cdot \boldsymbol{v}^* \rangle / (\langle \boldsymbol{v} \rangle \cdot \langle \boldsymbol{v}^* \rangle)$), this means that its value must be maximum at zero frequency, which leads to the plus sign in front of α_2^3.

C Theoretical limitation of the modeling

Now that the model in Eq. 2 and the additional terms it contains have been introduced, its corresponding limitation in terms of frequency must be estimated. We want to specify up to what frequency value, approximately, the low frequency approximation used still represents accurately the dynamic tortuosity. This limit is attained when the terms of higher order are not small anymore, compared with the retained terms. In Appendix A we write the actual Laurent-series for the dynamic tortuosity:

$$\alpha(\omega) = \frac{\omega_v}{\mathrm{j}\omega} + \alpha_0 + \alpha_1^2 \left(-\frac{\mathrm{j}\omega}{\omega_v}\right) + \alpha_2^3 \left(-\frac{\mathrm{j}\omega}{\omega_v}\right)^2 + \alpha_3^4 \left(-\frac{\mathrm{j}\omega}{\omega_v}\right)^3 + \alpha_4^5 \left(-\frac{\mathrm{j}\omega}{\omega_v}\right)^4 + \mathcal{O}\left(\frac{\mathrm{j}\omega}{\omega_v}\right)^5 \tag{10}$$

and show how the characteristic viscous frequency ω_v and dimensionless form-factors parameters α_p^{p+1}, $p = 0, 1, 2, \ldots$, are determined in principle from the microgeometry. For Eq. 2 to remain accurate, we may estimate that the terms with α_3^4 and α_4^5 in (10) should not exceed 5% of those with α_1^2 and α_2^3. This yields the following frequency ranges:

$$\begin{aligned} &\omega < \sqrt{0.05 \frac{\alpha_1^2}{\alpha_3^4}}\omega_v \text{ for the imaginary part of } \alpha(\omega), \\ &\omega < \sqrt{0.05 \frac{\alpha_2^3}{\alpha_4^5}}\omega_v \text{ for the real part of } \alpha(\omega). \end{aligned} \tag{11}$$

If we had asked that the terms with α_1^2 and α_2^3 should not exceed 5% of the first ($\omega_v/\mathrm{j}\omega$) and second ($\alpha_0$) terms, we would have found the frequency ranges:

$$\begin{aligned} &\omega < \sqrt{0.05 \frac{1}{\alpha_1^2}}\omega_v \text{ for the imaginary part of } \alpha(\omega), \\ &\omega < \sqrt{0.05 \frac{\alpha_0}{\alpha_2^3}}\omega_v \text{ for the real part of } \alpha(\omega). \end{aligned} \tag{12}$$

If the geometry is simple enough, these should be comparable to the previous ones, while less severe: the convergence radius being finite, the need to add monomials in the series should accelerate as the frequency increases, which means that the corrections made by successive monomials remain significant only for smaller and smaller frequency increases. The conditions (11) are thus a priori more severe than (12). For circular cylindrical pores, as an example of simple geometry, we find successively for the above frequency ranges (with the values α_p^{p+1}, $p = 0, 1, 2$ given in Appendix A): $\omega < 0.8\omega_v$, $\omega < 0.76\omega_v$, $\omega < 0.95\omega_v$, $\omega < 2.12\omega_v$, which allows us to appreciate, in this case, how much (11) are more severe than (12).

In the experiments that were performed in this work, an estimation of ω_v was first provided. We could not use the conditions (11) because of our lack of knowledge of the parameters α_3^4 and α_4^5. An estimation of α_1^2 and α_2^3 was nevertheless obtained, retaining in the signals the frequencies $\omega < 0.8\omega_v$. Then, as we had no information on α_3^4 and α_4^5, we only verified, a posteriori, that the conditions (12) were satisfied with the obtained values of α_0, α_1^2 and α_2^3. In case of failure, the inference process was repeated by adapting the retained frequencies in the signals, until the criteria (12) were satisfied a posteriori. Here, we have observed that, starting with $\omega < 0.8\omega_v$, no iteration was necessary to perform for materials M1 and M3, whereas just

one iteration was necessary for M2 to satisfy the criteria (12).

D The Transmission operator

In the present study, the propagation of waves inside porous media is of main interest and the focus is put on the transmitted waves. Therefore, we need to determine an expression of the transmission operator $\tilde{T}(t)$, that describes the relationship between incident ($p^i(x,t)$) and transmitted ($p^T(x,t)$) waves, through the convolution

$$p^T(L,t) = \int_0^t \tilde{T}(\tau) p^i(0, t-\tau)\, \mathrm{d}\tau, \tag{13}$$

where L is the material width and 0 is the origin where the material starts. Experiments are performed in a guide having a diameter of 5 cm. The experimental set up is given in Fig. 1. Since pulses of frequencies as low as 70 Hz and as high as 3 kHz are used in the experiments, a length of 3 m of the pipe is used in the higher frequency range ($f > 1$ kHz), while a pipe length of 50 m is used otherwise. In the latter case, the pipe can be rolled to save space without perturbations on experimental signals (the cut-off frequency of the tube is $f_{\text{c-o}} = 4$ kHz). A sound source driver unit "Brand" made by a Realistic 40-9000 loudspeaker is used. Bursts are provided by a synthesized function generator (Standford Research Systems, model DS345-30MHz). The signals are amplified and filtered using a Standford Research Systems SR 650-Dual channel filter. The incident and transmitted signals are measured using the same microphone (Bruel and Kjaer, 4190) in the same position in the pipe. The incident signal is measured in the absence of any porous sample, while the transmitted signal is measured in the presence of the porous sample.

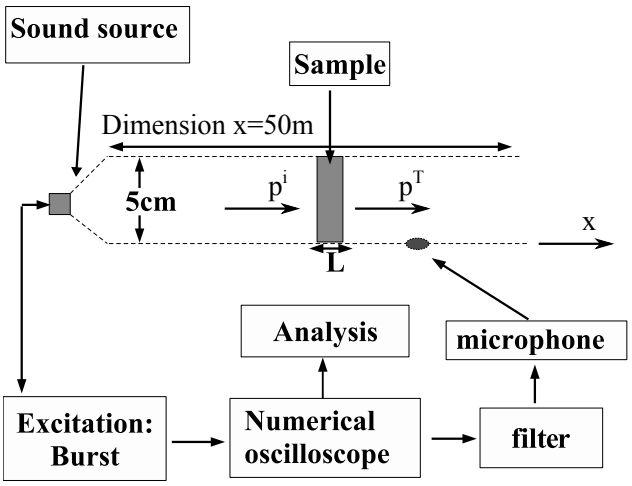

Figure 1: Schematic of the experimental apparatus used to measure the transmitted waves

When the incident pressure wave is normal to the material, one can obtain the transmission coefficient by solving a system composed of 4 equations (see Appendix B), obtained by considering continuity of pressure and velocity on each side of the material. Solving the system yields the transmission coefficient $T(\omega)$ in the frequency domain as

$$T(\omega) = \frac{2\Xi}{2\Xi \cosh(\mathrm{j}\omega L \xi_m) + (1+\Xi)^2 \sinh(\mathrm{j}\omega L \xi_m)}, \tag{14}$$

with L the material width, and

$$\Xi = \phi \sqrt{\frac{\beta(\omega)}{\alpha(\omega)}}, \quad \xi_m = \sqrt{\frac{\rho_f}{K_f} \alpha(\omega)\beta(\omega)}. \tag{15}$$

Now that the transmission coefficient has been worked out, the transmission operator can be obtained through

Fourier transform. We can thus carry on with the sensitivity analysis of the newly introduced parameters.

E Sensitivity analysis

We show the effect of varying α_0, α_1, α_2, α_0' and k_0' in synthetically generated transmitted signals, to compare the influence of visco-inertial and thermal parameters of equivalent order in the respective Laurent series of $\alpha(\omega)$ and $\beta(\omega)$. To do so, an experimentally measured incident signal is used as input, with a frequency band of $1000 - 2500\,\mathrm{Hz}$. The transmission coefficient of a test material is calculated using Eq. 14, and the transmitted signal is calculated through the convolution described in Eq. 13.

The other intrinsic parameters are arbitrarily fixed as: material width $L = 5\,\mathrm{cm}$, $\phi = 0.99$, $k_0 = 0.93 \cdot 10^{-9}\,\mathrm{m}^{-2}$ (or equivalently, the static flow resistivity $\sigma_0 = \eta/k_0 \approx 19750\,\mathrm{N.s.m}^{-4}$). The reference values are $\alpha_0 = 2.5$, $\alpha_0' = 2.3$, $\alpha_1 = \alpha_2 = 0$ and $k_0'/k_0 = 1.41$. The reason for this choice of k_0' is to set $\omega_v = \omega_\tau$ so that the comparison of the parameters influences remains fair. The general effects of varying the parameters are displayed on Figs.2–6, and summarized as follows:

- ▷ An increase in α_0 in Fig. 2 delays the transmitted signal, but increases its amplitude. The signal delay can be explained through the examination of the effective sound speed c_m inside the porous medium

$$c_m = \frac{c_0}{\sqrt{\alpha(\omega)\beta(\omega)}}, \tag{16}$$

  where c_0 is the sound celerity in ambient air. Increasing α_0 decreases c_m, producing the delay. At the same time, we note that c_m is increasing as a function of the frequency (since $\alpha(\omega)$ and $\beta(\omega)$ are both decreasing as a function of the frequency when $\omega < \omega_v$ and $\omega < \omega_\tau$). An increase in α_0 leading to a decrease in c_m is thus seen as a effective decrease in frequency, which results in a higher transmission. The thermal term having a similar order in the Laurent series of $\beta(\omega)$ is γ, which is not subject to variation.

- ▷ An increase in α_1, seen in Fig. 3, decreases the transmitted signal's amplitude, with a dispersionless phenomenon. This is coherent with its interpretation as a diminution of the effective permeability, as seen in Eq. 8: a permeability decrease (resistivity increase) is bound to reduce the wave transmission in the material. Little to no effect on the transmitted wave phase is perceived, as expected since the apparent permeability $k_{0\,\mathrm{app}}(\omega)$ of Eq. 8 mostly takes into account diffusive, dispersionless processes. The thermal term having a similar order in the Laurent series of $\beta(\omega)$ is k_0'. The influence of increasing k_0' is displayed in Fig. 4, where it is seen that increasing values of k_0' increase the amplitude of the transmitted signal, with almost no influence on the signal phase.

- ▷ The influence of α_2 is shown in Fig. 5: increasing the value of α_2 leads to a decreasing transmitted wave amplitude. The signal phase is also shifted, resulting in a faster wave inside the porous medium. As expected from Eq. 9, an increase in α_2 results in a faster decrease in the apparent inertial factor $\alpha_{0\,\mathrm{app}}(\omega)$. It is thus coherent to observe a trend opposite the one shown in Fig. 2 for the influence of α_0, where an increase in α_0 leads to a general increase in the transmitted wave amplitude, and its delay. The thermal term having a similar order in the Laurent series of $\beta(\omega)$ is α_0'. An increase in α_0', while barely seen in Fig. 6, increases the amplitude of the signal, but does not delay it.

The conclusion of this sensitivity analysis is that the influence of the additional parameters α_1 and α_2 has been shown significant, which motivates the need for an inverse method of identification to retrieve their values. This study was also conducted on synthetically generated materials of higher and lower static viscous permeabilities, yielding similar conclusions, provided that the frequency content of the incident waves is adapted, since ω_v and ω_τ are functions of k_0.

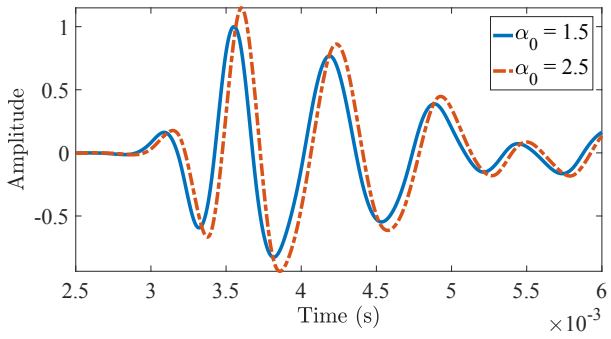

Figure 2: Influence of α_0 on transmitted waves

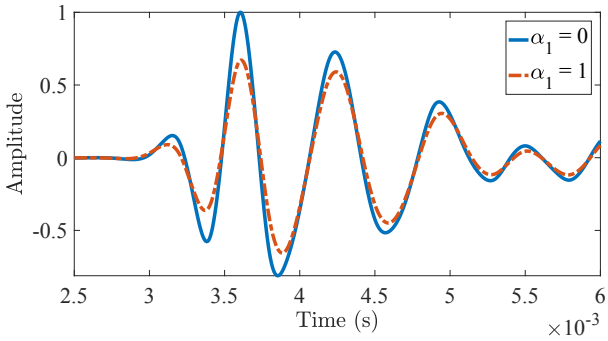

Figure 3: Influence of α_1 on transmitted waves

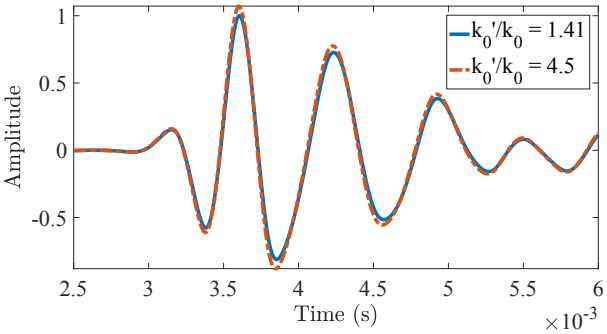

Figure 4: Influence of k_0' on transmitted waves

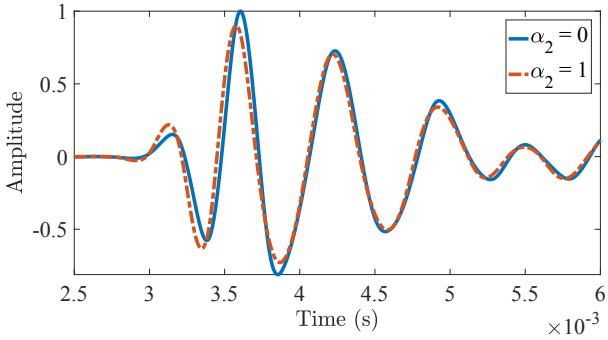

Figure 5: Influence of α_2 on transmitted waves

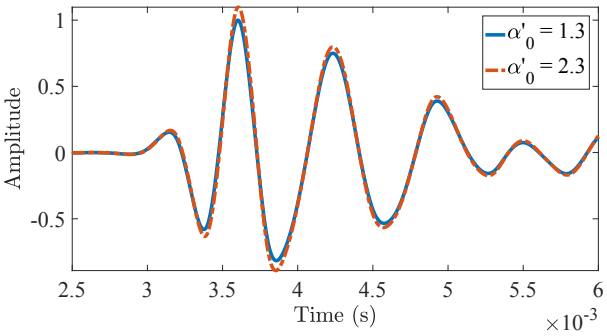

Figure 6: Influence of α_0' on transmitted waves

III Inverse problem: statistical inference

In the context of inverse problems for parameter estimation, statistical inference in the Bayesian framework consists in recasting parameters of interest as random variables associated with probability densities encompassing established information or new information collected through measurements [31, Chap. 8]. A general review on inverse problem theory can be found in [32], while a review on statistical inverse problems can be found in [33]. Statistical inverse problems use the information contained in both the observed experimental data $\boldsymbol{d}^{\mathrm{e}}$ and the prior knowledge of the estimated parameters $\boldsymbol{m}$. In the present article, $\boldsymbol{d}^{\mathrm{e}}$ encompasses all the measured transmitted signals in the time domain being used for the inference, and $\boldsymbol{m} = (\phi,\, \alpha_0,\, \alpha_1,\, \alpha_2,\, \alpha_0',\, k_0,\, k_0'/k_0)$. These two states of information are combined to express our degree of knowledge about the true values of $\boldsymbol{m}$, improved thanks to the information contained in the observation $\boldsymbol{d}^{\mathrm{e}}$.

Using Bayes' theorem, a *posterior probability density* $\pi(\boldsymbol{m}|\boldsymbol{d}^{\mathrm{e}})$ is defined for the model parameters $\boldsymbol{m}$, given a set of observable parameters $\boldsymbol{d}^{\mathrm{e}}$. Formally, this writes

$$\pi(\boldsymbol{m}|\boldsymbol{d}^{\mathrm{e}}) = \frac{\pi(\boldsymbol{d}^{\mathrm{e}}|\boldsymbol{m})\,\pi(\boldsymbol{m})}{\pi(\boldsymbol{d}^{\mathrm{e}})}, \tag{17}$$

where $L(\boldsymbol{m}) \equiv \pi(\boldsymbol{d}^{\mathrm{e}}|\boldsymbol{m})$ is the *likelihood* function, $\pi(\boldsymbol{m})$ is the *prior density*, and $\pi(\boldsymbol{d}^{\mathrm{e}})$ is the *Bayesian evidence*. The marginal posterior probability $\pi(\boldsymbol{m}|\boldsymbol{d}^{\mathrm{e}})$ reflects all the information inferred on $\boldsymbol{m}$, conditional on the observation $\boldsymbol{d}^{\mathrm{e}}$, and is the quantity to be found. The evidence $\pi(\boldsymbol{d}^{\mathrm{e}})$ represents the probability of the experimental data being generated by the given parameters and models; the evidence is generally a term difficult to evaluate numerically: its calculation can be conveniently circumvented by means of the MCMC method detailed in Sec. C. The aforementioned terms are detailed in the following.

A Likelihood

The likelihood function represents the mechanism through which information provided by the observation is incorporated into the posterior density. The physical correlations between $\boldsymbol{m}$ and $\boldsymbol{d}^{\mathrm{e}}$, as predicted by a physical model (here a convolution between incident signal and transmission operator), are represented by a deterministic forward operator $\boldsymbol{G}$, and a noise $\boldsymbol{\epsilon}$ accounting for the uncertainty:

$$\boldsymbol{d}^{\mathrm{e}} = \boldsymbol{G}(\boldsymbol{m}^*) + \boldsymbol{\epsilon}, \tag{18}$$

where $\boldsymbol{m}^*$ is unknown. The components of $\boldsymbol{\epsilon}$ are assumed to be independent of the model parameters $\boldsymbol{m}$ and identically distributed random variables of zero mean Gaussian density π_ϵ.
The forward operator is represented in a discrete-time manner by noting $\boldsymbol{G}(\boldsymbol{m}) = (G_1(\boldsymbol{m}), \dots G_j(\boldsymbol{m}), \dots, G_{N_d}(\boldsymbol{m}))$ where N_d is the number of time steps observed in the experimental transmitted signal, and with

$$G_j(\boldsymbol{m}) = \int_0^{t_j} \tilde{T}(\boldsymbol{m}, \tau) p^i(x_{\mathrm{meas}},\, t_j - (x_{\mathrm{meas}} - L)/c_f - \tau)\mathrm{d}\tau, \tag{19}$$

with x_{meas} the location of the microphone, where the dependency on the parameters $\boldsymbol{m}$ has been made explicit in the writing of the transmission kernel and where t_j is the j^{th} observed time step. The likelihood takes the form

$$L(\boldsymbol{m}) = \pi_\epsilon(\boldsymbol{d}^{\mathrm{e}} - \boldsymbol{G}(\boldsymbol{m})), \tag{20}$$

which reads, assuming π_ϵ follows a zero mean Gaussian distribution,

$$L(\boldsymbol{m}) = \prod_{j=1}^{N_d} \frac{1}{\sqrt{2\pi\sigma_j^2}} \exp\left(-\frac{|\boldsymbol{d}^{\mathrm{e}} - G_j(\boldsymbol{m})|^2}{2\sigma_j^2}\right), \tag{21}$$

where σ_j^2 denotes the noise variance and is either determined experimentally, set a priori, or taken as a new variable to identify. The larger the value of σ_j^2, the larger the estimated uncertainty on the observation. The value of the standard deviation σ_j is taken in this work to 2% of the average of the absolute value of the considered experimental transmitted signal, to encompass our uncertainty in the acquisition chain, the material length, the experimental conditions (temperature, pressure, etc.) and the possible presence of gaps and leaks around the samples or the microphone. For numerical reasons, the logarithm of the likelihood is used instead of Eq. 21. As is the case for classical inverse problems where a cost function has to be minimized in order to retrieve the parameters of interest, the likelihood can be viewed as the probabilistic equivalent of such a quantity, effectively measuring the probability of the experience being observed, for a given set of parameters.

Parameter	ϕ	α_0	α_1	α_2	α'_0	$k_0(10^{-9}\,\mathrm{m}^2)$	$\sigma_0(10^3\,\mathrm{N.s.m}^{-4})$	k'_0/k_0
Prior Min	0.6	1.01	0	0	1.01	0.1	0.92	1
Prior Max	0.99	4	3	3	4	20	183.7	20

Table 1: Prior boundaries

B Prior model

The prior probability $\pi(\boldsymbol{m})$ incorporates the information obtained on the model parameters independently of the observation $\boldsymbol{d}^{\mathrm{e}}$ used during the inference. It reflects the user's prior insight into the problem, generalizing the classical constraints used during deterministic inversion, assigning weights to the more probable values. When no prior information is available or if prior modeling is of questionable accuracy, a wide-range, non-informative improper homogeneous density on the parameters supports represents well one's ignorance and merely sets boundaries for each parameter, as in classical deterministic inverse problems. In the present article, prior independence is first assumed among the unknown parameters, setting

$$\pi(\boldsymbol{m}) = \prod_{i=1}^{8} \pi_i(m_i), \tag{22}$$

where a uniform probability $\pi_i(m_i) \sim \mathcal{U}(m_{i,\min}, m_{i,\max})$ is assumed for the priors, with $m_{i,\min}$ and $m_{i,\max}$ the boundaries, given in Table 1. It is possible to see [7, 29, 5, 34] that, whatever the pore geometry considered,

$$\alpha_0 \geq \alpha'_0 > 1; \;\; k_0 \leq k'_0. \tag{23}$$

The equalities are satisfied only for the case of aligned cylindrical pores. As a result, the constraints can be further integrated into the prior by assigning null probabilities to the parameters not respecting these conditions.

C MCMC: posterior sampling

As the posterior probability density defined in Eq. 17 is only known up to a normalizing constant, it is still necessary to devise a technique to draw samples directly from the posterior distribution, without having to calculate the Bayesian evidence, which is especially arduous in high-dimensional parameter spaces. To address this issue, a technique called Markov Chain Monte Carlo (MCMC) is exploited. A random-walk algorithm is designed to explore the posterior density, moving preferentially towards regions of high probability densities, efficiently exploring the area of interest (usually small compared with the parameter space generated by the prior support) and creating a Markov chain whose stationary distribution is the distribution of interest. This is done with a Metropolis-Hasting [35, 36] algorithm for the selection process, consisting in an acceptance/rejection step that creates the transition kernel of the Markov chain. The reader is referred to [35, 36, 37, 38] for the specifics, including that of the MCMC strategy used in the present article (coined MT-DREAM_ZS [38]).

In the present work, 3 Markov chains are used in parallel, on which 10^5 iterations are performed, with the first 10% of each chain being discarded as burn-in to allow decorrelation with the initial samples. The chains are initialized by sampling from the prior's support. Convergence is checked a posteriori, through a Gelman-Rubin diagnostic [39] and a visual check of the chain samples.

IV Identification results

In this section, the inference method is carried on three different porous materials, coined M1, M2 and M3. For each of them, a dedicated discussion is provided. The Maximum A Posteriori (MAP) estimator is chosen as the reference probabilistic estimator in this study, since it is closest in meaning to the estimates obtained through usual deterministic methods, related to a maximum likelihood estimation. The MAP estimate $\boldsymbol{m}_{\mathrm{MAP}}$ is defined as

$$\boldsymbol{m}_{\mathrm{MAP}} = \arg\max_{\boldsymbol{m}} \pi(\boldsymbol{m}|\boldsymbol{d}^{\mathrm{e}}). \tag{24}$$

The conditional mean estimator $\mathbb{E}(m_i|\boldsymbol{d}^{\mathrm{e}})$ is also given in the results summaries. The inference results are summarized in Tables 2,3 and 4 for inferences of materials M1, M2, and M3, respectively, where the MAP and the mean are reported. The 95% credibility intervals (CI) are also given, since they carry more meaning when the identified parameter does not follow a normal distribution. In the Bayesian sense, such an interval is interpreted as a 95% probability that the true value of a given parameter falls within the credible region. The waves transmitted by materials M1, M2 and M3 are measured using incident pressure signals whose frequency spectra are centered in a frequency range of $[50\,\mathrm{Hz} - 2\,\mathrm{kHz}]$, depending on the estimated characteristic angular frequency ω_v of the materials, the newly developed acoustical model being dedicated to the low frequency regime. We illustrate the shape of the reference and transmitted signals (material M2) in the time domain for two different frequency contents, in Figs. 7-8. As the frequency increases, it becomes apparent that the transmitted signal is delayed.

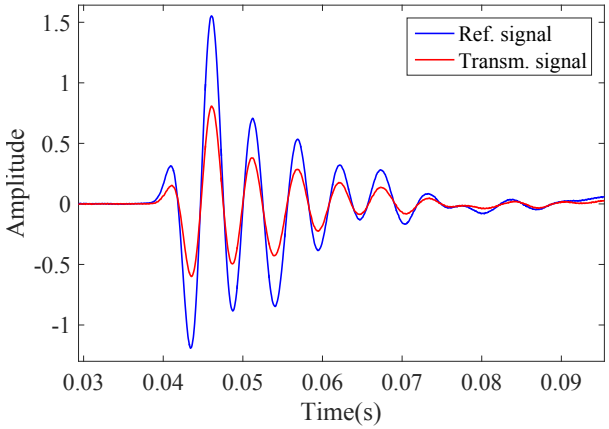

Figure 7: Reference and transmitted signals for a frequency content centered around 70 Hz

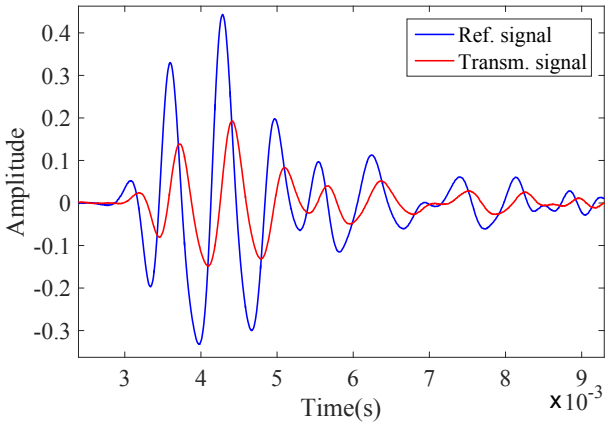

Figure 8: Reference and transmitted signals for a frequency content centered around 2 kHz

Figures 9,11 and 13 show the probability density functions (pdf, diagonal elements of the matrix plot) and joint-pdfs (off-diagonal elements) inferred on material M1, M2 and M3, respectively. Obtaining the pdf is achieved through a Kernel density estimation of the Markov-Chains resulting from the MCMC simulations, for each parameter. The 2D joint-pdf is calculated by first binning the scatter plot of each parameter pair, calculating the associated 3D histogram and then applying a surface plot to display the binned areas, with warmer colors corresponding to higher probability densities. The goal of such a plot is to see the shape of the densities and the density support range of the sampled MCMC elements. It can also be used to describe the type of correlations that exist between the parameters for a specific inverse problem.

Finally, the identification is concluded by showing the agreement, both in time– and frequency–domains, between experimental and MAP signals, in Figures 10, 12 and 14, for materials M1, M2 and M3, respectively.

A Inference of M1 properties

Material M1 is a melamine-like foam, of high porosity and low resistivity and of thickness $L = 5\,\text{cm}$. Previous experiments, using reference techniques [40, 9, 41, 10, 14], showed a porosity of 0.98 ± 0.02 and a flow resistivity of $6000 \pm 1000\text{N.s.m}^{-4}$, which is close to the present results.

We note that the new parameters, α_1 and α_2, are correctly identified (i.e, they display an informative posterior probability density). This is further proof of the importance of these parameters for the considered experiment. If they had not been taken into account, their contribution to the acoustic response would have been absorbed during the inference by other parameters, which would have in turn biased their identification.

Looking at Fig. 10, we see that the fit between experimental and MAP signals is excellent, even for signals that were not used during the inference, where the frequency content extends beyond the characteristic frequency for viscous effects ($\omega_v \approx 4018\,\text{rad.s}^{-1}$, $f_v \approx 639\text{Hz}$). The purpose of showing a fit between an experimental signal that was not used during the inference and with a frequency content higher than the theoretical limit of our model is to test the extended validity of our model.

Parameter	ϕ	α_0	α_1	α_2	α_0'	$k_0(10^{-9}\,\text{m}^2)$	$\sigma_0(10^3\,\text{N.s.m}^{-4})$	k_0'/k_0
Inverted value (MAP)	0.99	1.27	0.17	0.14	1.16	3.76	4.88	2
Mean	0.98	1.29	0.15	0.13	1.13	3.77	4.88	2.03
Lower 95% CI	0.96	1.22	0.02	0.01	1.01	3.43	4.43	1.36
Upper 95% CI	0.99	1.37	0.25	0.27	1.26	4.15	5.36	2.82

Table 2: Results summary for the inference of M1 parameters.

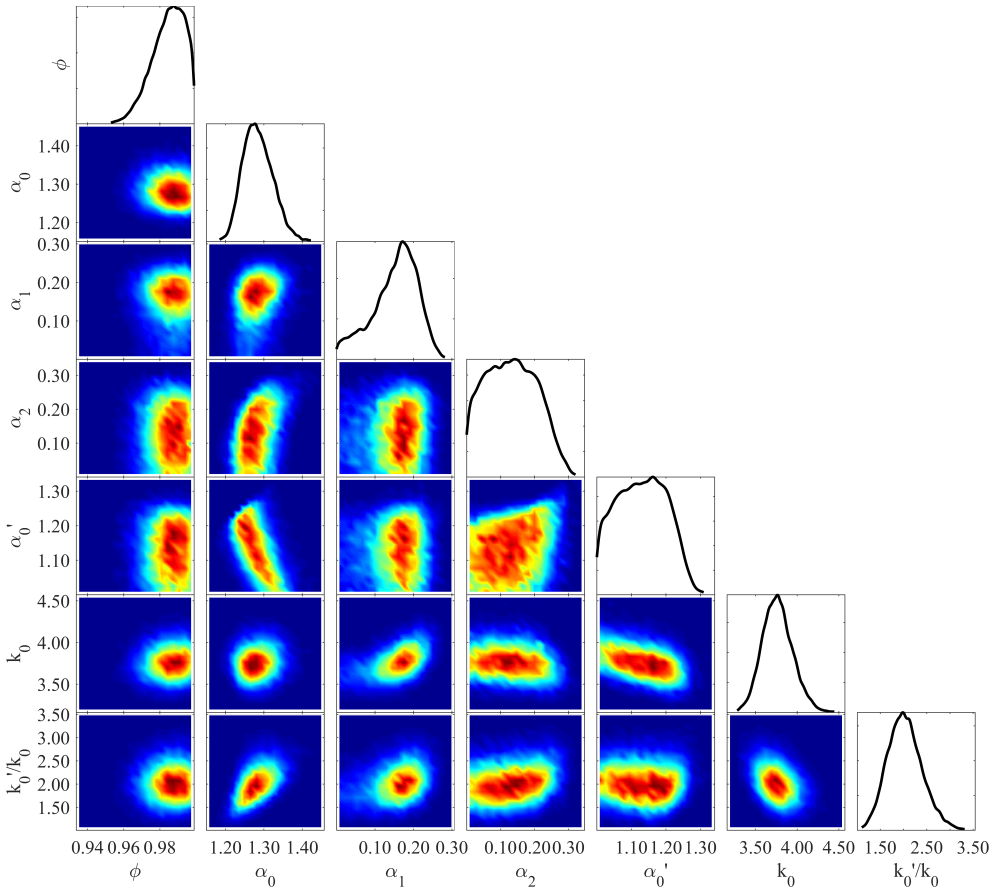

Figure 9: (Color online) M1 inference pdfs (diagonal elements), scatter and joint pdfs (off-diagonal elements).

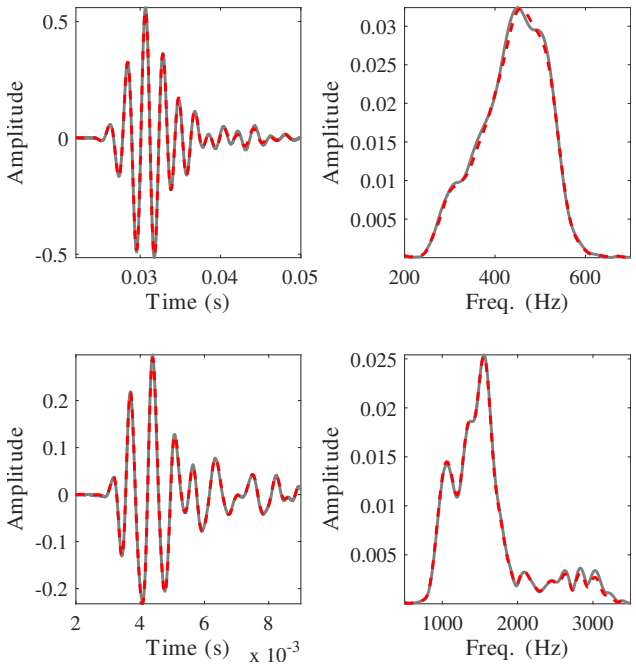

Figure 10: (Color online) Material M1. MAP estimates (dashed line) and experimental signals (solid line). Left: time signals. Right: frequency spectrum.

B Inference of M2 properties

Material M2 is the tested sample with the lowest static permeability (highest flow resistivity), and consists of a foam of thickness $L = 2.5\,\text{cm}$. Previous experiments, using reference techniques [40, 9, 41, 10, 14], showed a porosity of about 0.84 ± 0.05 and a flow resistivity of $36000 \pm 6000\text{N.s.m}^{-4}$, which is close to the present results. The inertial factor was estimated in a previous study [17] at $\alpha_0 = 2.15 \pm 0.15$, but since α_2 had not been taken into account at the time, it is consistent with obtaining a value of α_0 that is higher. Once again, we immediately note that α_1 and α_2 present a non-uniform probability density, meaning that some information has been extracted from the inference signals.

An interesting additional piece of information that can be drawn from the joint-pdfs (off-diagonal elements on Fig. 11) concerns the correlation between parameters. A joint-pdf of elliptical shape indicates a correlation between the associated two parameters. The slope sign of the ellipse's major axis informs on the correlation sign. These correlations need not be understood as physical correlations between parameters. They depend on the problem structure and the models used. However, they dispense useful information since they can help predict the impact of fixing a parameter's value on the inference of the other parameters. For instance, consider the static viscous permeability to be fixed during the inversion, without taking any uncertainty into account. If the value is above the MAP estimate found in Table 3, then the identified values of α_1 would be increased. This is due to the positive correlations between k_0 and and α_1, as seen in Fig. 11, line 6, column 3.

Looking at Fig. 12, we see that the fit between experimental and MAP signals is good, even at frequencies close to the characteristic frequency for viscous effects ($\omega_v \approx 23571\,\text{rad.s}^{-1}$, $f_c \approx 3751\text{Hz}$). The characteristic frequency is larger for resistive materials, where the transition to the inertial regime is attained at higher frequencies. The discrepancies between signals seem greater than for material M1 for instance, mostly because the high resistivity of this material made the signal to noise ratio poorer during the experiments. Note that during the inference, only signals having a frequency content below 1000 Hz were used, to respect the limit conditions given by relations 12.

Parameter	ϕ	α_0	α_1	α_2	α_0'	$k_0(10^{-9}\,\mathrm{m}^2)$	$\sigma_0(10^3\,\mathrm{N.s.m}^{-4})$	k_0'/k_0
Inverted value (MAP)	0.80	2.62	0.85	0.18	2.34	0.52	35.5	3.72
Mean	0.80	2.58	0.68	0.29	2.20	0.52	35.4	3.45
Lower 95% CI	0.70	2.34	0.07	0.01	1.43	0.50	34.2	1.61
Upper 95% CI	0.89	2.72	1.16	0.71	2.60	0.54	36.6	4.6

Table 3: Results summary for the inference of M2 parameters.

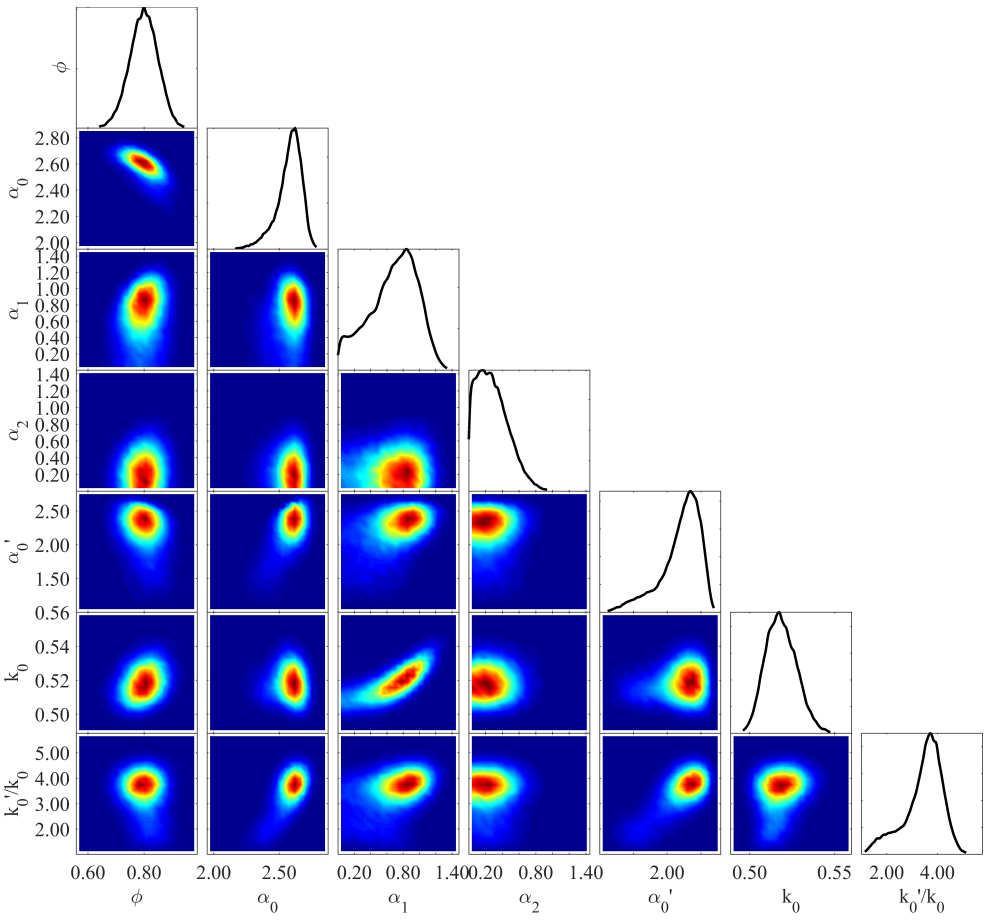

Figure 11: (Color online) M2 inference pdfs (diagonal elements), joint pdfs (off-diagonal elements).

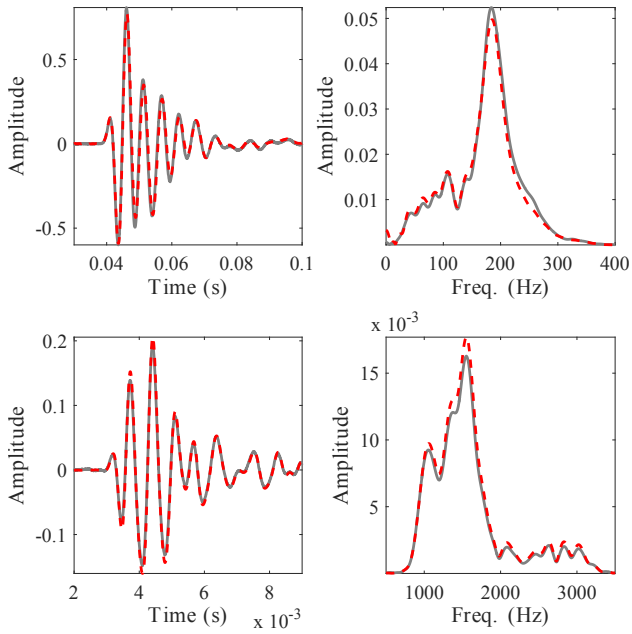

Figure 12: (Color online) Material M2. MAP estimates (dashed line) and experimental signals (solid line). Left: time signals. Right: frequency spectrum.

C Inference of M3 properties

Material M3, of thickness $L = 20.2\,\text{cm}$, is a high porosity, high flow permeability foam material. Its porosity and flow resistivity have been estimated using reference techniques [40, 9, 41, 10, 14], yielding $\phi = 0.98 \pm 0.02$, $\sigma_0 = 7000 \pm 2000\text{N.s.m}^{-4}$, which is coherent with the inferred values.

The results in Table 4 suggest that the value of α_1 is close to 0, but this should be taken cautiously since it appears that the parameter has a large credibility interval. We also note that the identification of parameter α_2 is unique in this work, since its pdf (shown in Fig. 13) displays a bi-modal probability density function. This indicates the presence of two likely values for α_2, having observed this particular set of data. From a technical point of view, the inference of multi-modal probability density functions is quite challenging. It has been made possible here thanks to the MCMC strategy used in this work (see Sec. C).

Looking at Fig. 14, we see that the fit between experimental and MAP signals is excellent. The characteristic viscous angular frequency is $\omega_v \approx 5247\,\text{rad.s}^{-1}$ ($f_c \approx 835\text{Hz}$).
When performing the inference, we noted that low flow resistivity materials (high static permeability) could be more challenging to identify, due to the lower value of their characteristic angular frequency ω_v, which in turn constrained the use of lower frequencies. Increasing the material thickness (as for M3) proved useful, since it made the beginning of the inertial regime more pronounced even at very low frequencies, while still displaying correct signal to noise ratios. We thus recommend that any future similar work start by evaluating the characteristic frequency of the material (through prior knowledge of its resistivity, which is often a parameter readily available), and that the material thickness be maximized while keeping a good signal to noise ratio near the maximum frequencies used for the inference, respecting the constraint given in Eq. 12.

Parameter	ϕ	α_0	α_1	α_2	α_0'	$k_0(10^{-9}\,\mathrm{m}^2)$	$\sigma_0(10^3\,\mathrm{N.s.m}^{-4})$	k_0'/k_0
Inverted value (MAP)	0.98	1.76	0.07	0.66	1.62	2.85	6.44	4.34
Mean	0.98	1.77	0.31	0.59	1.57	2.85	6.44	4.39
Lower 95% CI	0.96	1.68	0.01	0.08	1.32	2.82	6.36	3.72
Upper 95% CI	0.99	1.89	0.76	0.99	1.75	2.89	6.51	5.1

Table 4: Results summary for the inference of M3 parameters.

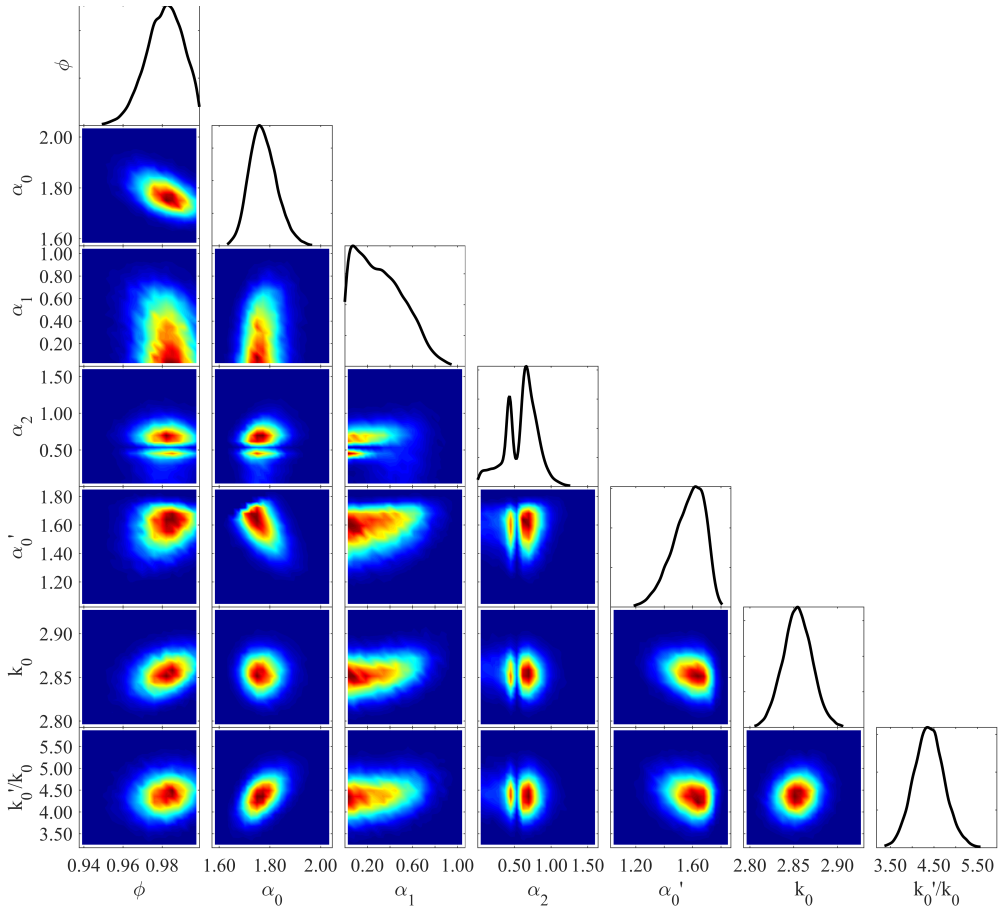

Figure 13: (Color online) M3 inference pdfs (diagonal elements), joint pdfs (off-diagonal elements).

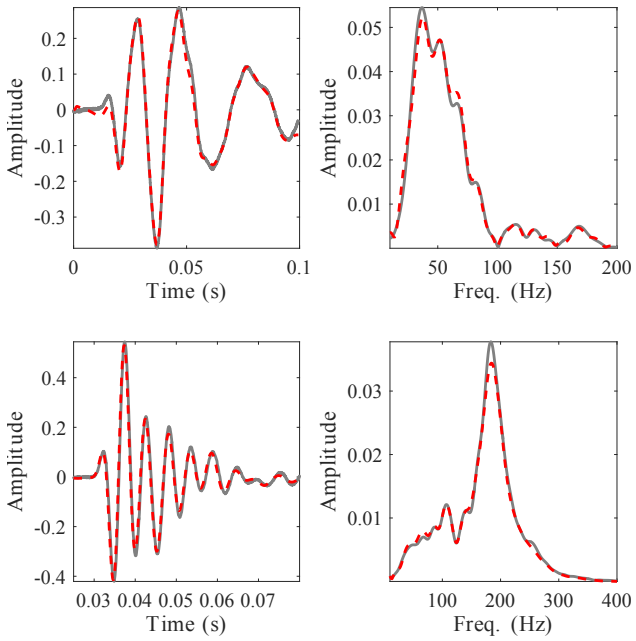

Figure 14: (Color online) Material M3. MAP estimates (dashed line) and experimental signals (solid line). Left: time signals. Right: frequency spectrum.

V Conclusion

The modeling of wave propagation inside porous media and the non invasive determination of their microstructure are crucial for the diverse research fields in which porous materials are studied. This article has introduced a model extension for the description of wave propagation in porous media in the low-mid frequency regime, corresponding to frequencies lower than a certain fraction of the characteristic angular frequency ω_v, which depends on the material properties. Two additional intrinsic parameters have been introduced, α_1 and α_2, related to the visco-inertial behavior of the fluid phase. The first result of this work is that the visco-inertial parameters α_1 and α_2 have a significant influence on the acoustical response of the material. Their effects on the transmitted waves have been detailed, and a physical interpretation has been given:

- ▷ Parameter α_1 is associated with the transition of the viscous regime as the frequency increases, and intervenes in the definition of an apparent permeability of decreasing values as the frequency increases (increasing flow resistivity of the material).
- ▷ Parameter α_2 is associated with the transition of the inertial regime as the frequency increases, and intervenes in the definition of an apparent inertial factor of decreasing values as the frequency increases.

The work has also proposed a statistical inference method based on Bayes theorem to identify simultaneously the 7 parameters intervening in the newly developed modeling, using low-mid frequency range signals in the time domain, measured in a transmission experiment adapted for low frequency waves. The inference process was carried out on three different porous materials in the low to high static permeability range (high to low flow resistivity), showing the capability of first level Bayesian inference to yield one's knowledge on the inferred material properties, given a certain set of observations and associated uncertainties. Setting a suitable limit to the frequencies that must be used during the inference remains a delicate issue. If set too high the model is insufficient; if set too low, the effect of higher order parameters is very small and the influence of systematic errors and noise in the signal prevents making accurate identifications. Approximate frequency

conditions have been developed, and an iterative procedure has been conducted during the inference to ensure that the prescribed conditions were indeed imposed.
The main result of this work is that in all cases, the parameters α_1 and α_2 have been successfully identified, as shown by their informative posterior density. Had they not been taken into account, the inferred values of the other parameters would have changed, in particular those of the static viscous permeability k_0 (or flow resistivity σ_0) and of the inertial factor α_0. It is thus recommended that future low frequency acoustic inverse measurements take α_1 and α_2 into account.

The present work is the first, to the authors' knowledge, to provide a range of values for the newly defined parameters α_1 and α_2, as well as an identification framework that can simultaneously yield the porosity, static viscous and thermal tortuosities and static viscous and thermal permeabilities.

A Definition of the model parameters from microstructure and application to the case of cylindrical circular pores

Based on the idealization that the fluid flow is incompressible at the pore scale, we wish to find the macroscopic level dynamic permeability and dynamic tortuosity response factors $k(\omega)$ and $\alpha(\omega)$, such that:

$$\phi \langle \boldsymbol{v} \rangle = -\frac{k(\omega)}{\eta} \nabla \langle p \rangle , \quad \rho_f \alpha(\omega) \frac{\partial \langle \boldsymbol{v} \rangle}{\partial t} = -\nabla \langle p \rangle , \tag{25}$$

where $\langle\rangle$ denotes volume average in the fluid domain V_f, $\boldsymbol{v}$ and p are the fluid velocity and excess pressure, ϕ is the porosity, and ρ_f and η are the fluid ambient density and viscosity. At the microscopic level (with ∂V the pore walls) the idealization of incompressible flow motion allows us to write:

$$\rho_f \mathrm{j}\omega \boldsymbol{v} = -\nabla p + \eta \Delta \boldsymbol{v}, \text{ in } V_f \tag{26}$$

$$\nabla \cdot \boldsymbol{v} = 0, \text{ in } V_f \tag{27}$$

$$\boldsymbol{v} = \boldsymbol{0}, \text{ on } \partial V. \tag{28}$$

The compatibility between the macroscopic description (25) and the microscopic description (26-28) then immediately gives the following prescription for calculating $k(\omega)$ and $\alpha(\omega)$:

1. Solve the following microscopic problem: (to write this problem, substitute in (26-28), $\eta \boldsymbol{v} = \frac{\Delta p}{\Delta L} \boldsymbol{w}$ and $-\nabla p = \frac{\Delta p}{\Delta L}(\boldsymbol{e} - \nabla \pi)$, with $\boldsymbol{e}$ a unit vector in the direction of macroscopic flow and Δp the macroscopic pressure drop over a distance ΔL; π, therefore, is a fluctuating scaled pressure part with no macroscopic gradient, that is, a stationary random field in stationary random geometries, or a periodic field in periodic geometries)

$$-\frac{\mathrm{j}\omega}{\nu} \boldsymbol{w} - \nabla \pi + \Delta \boldsymbol{w} + \boldsymbol{e} = 0, \text{ in } V_f \tag{29}$$

$$\nabla \cdot \boldsymbol{w} = 0, \text{ in } V_f \tag{30}$$

$$\pi \text{ stationary (periodic in periodic geometries), in } V_f \tag{31}$$

$$\boldsymbol{w} = \boldsymbol{0}, \text{ on } \partial V. \tag{32}$$

2. Perform the average $\langle \boldsymbol{w} \rangle$ of the solution $\boldsymbol{w}$. Then $k(\omega)$ and $\alpha(\omega)$ satisying (25) are given by

$$k(\omega)/\phi = \langle \boldsymbol{w} \rangle \cdot \boldsymbol{e}, \quad \alpha(\omega) = \nu\phi/\mathrm{j}\omega k(\omega). \tag{33}$$

The solution $\boldsymbol{w}$ to the problem (29-32) is a *unique* stationary field thanks to the important condition (31).

The stationary solution π is unique if taken of zero mean (i.e. $\langle\pi\rangle = 0$ or also $\langle\pi\boldsymbol{w}\rangle = 0$).

At low-enough frequencies the scaled velocity solution $\boldsymbol{w}$ and the associated fluctuating scaled pressure π will be power series expansions (we explicitly justify it later)

$$\boldsymbol{w} = \boldsymbol{w}_0 + \frac{-\mathrm{j}\omega}{\nu}\boldsymbol{w}_1 + \left(\frac{-\mathrm{j}\omega}{\nu}\right)^2 \boldsymbol{w}_2 + \dots \tag{34}$$

$$\pi = \pi_0 + \frac{-\mathrm{j}\omega}{\nu}\pi_1 + \left(\frac{-\mathrm{j}\omega}{\nu}\right)^2 \pi_2 + \dots \tag{35}$$

Substituting (34) in (33) we find

$$k(\omega)/\phi = \langle\boldsymbol{w}\rangle\cdot\boldsymbol{e} = \langle\boldsymbol{w}_0\rangle\cdot\boldsymbol{e} + \frac{-\mathrm{j}\omega}{\nu}\langle\boldsymbol{w}_1\rangle\cdot\boldsymbol{e} + \left(\frac{-\mathrm{j}\omega}{\nu}\right)^2\langle\boldsymbol{w}_2\rangle\cdot\boldsymbol{e} + \left(\frac{-\mathrm{j}\omega}{\nu}\right)^3\langle\boldsymbol{w}_3\rangle\cdot\boldsymbol{e} + \dots \tag{36}$$

and by (35), after straightforward calculations, we obtain the following low-frequency Laurent series expansion:

$$\begin{aligned}\alpha(\omega) = \frac{\nu\phi}{\mathrm{j}\omega k(\omega)} &= \left(\frac{\omega_v}{\mathrm{j}\omega} \equiv \frac{\nu}{\mathrm{j}\omega\left(\langle\boldsymbol{w}_0\rangle\cdot\boldsymbol{e}\right)}\right) + \left[\alpha_0 \equiv \frac{\langle\boldsymbol{w}_1\rangle\cdot\boldsymbol{e}}{\left(\langle\boldsymbol{w}_0\rangle\cdot\boldsymbol{e}\right)^2}\right] \\ &+ \left[\alpha_1^2 \equiv \frac{\langle\boldsymbol{w}_2\rangle\cdot\boldsymbol{e}\,\langle\boldsymbol{w}_0\rangle\cdot\boldsymbol{e} - \left(\langle\boldsymbol{w}_1\rangle\cdot\boldsymbol{e}\right)^2}{\left(\langle\boldsymbol{w}_0\rangle\cdot\boldsymbol{e}\right)^4}\right]\left(\frac{-\mathrm{j}\omega}{\omega_v}\right) \\ &+ \left[\alpha_2^3 \equiv \frac{\langle\boldsymbol{w}_3\rangle\cdot\boldsymbol{e}\left(\langle\boldsymbol{w}_0\rangle\cdot\boldsymbol{e}\right)^2 - 2\langle\boldsymbol{w}_2\rangle\cdot\boldsymbol{e}\,\langle\boldsymbol{w}_1\rangle\cdot\boldsymbol{e}\,\langle\boldsymbol{w}_0\rangle\cdot\boldsymbol{e} + \left(\langle\boldsymbol{w}_1\rangle\cdot\boldsymbol{e}\right)^3}{\left(\langle\boldsymbol{w}_0\rangle\cdot\boldsymbol{e}\right)^6}\right]\left(\frac{-\mathrm{j}\omega}{\omega_v}\right)^2 + \dots\end{aligned} \tag{37}$$

where the sign $\equiv$ stands for 'identically equal to'. Each partial solution field $\boldsymbol{w}_n$ of order $n = 1, 2, 3, \dots$ can be computed from the preceding $\boldsymbol{w}_{n-1}$ by solving the following recursive problem that results from the substitution of the expansions (34-35) in (29-32) and the identification of terms of same $(-\mathrm{j}\omega/\nu)$ power (for shortness, the mentions "in V_f" or "on ∂V" are omitted):

$$\Delta\boldsymbol{w}_n = \nabla\pi_n - \boldsymbol{w}_{n-1} \tag{38}$$

$$\nabla\cdot\boldsymbol{w}_n = 0 \tag{39}$$

$$\pi_n \text{ stationary (periodic in periodic geometries)} \tag{40}$$

$$\boldsymbol{w}_n = 0 \tag{41}$$

The initialization of the calculation is the determination of the first partial field solution $\boldsymbol{w}_0$:

$$-\Delta\boldsymbol{w}_0 = -\nabla\pi_0 + \boldsymbol{e} \tag{42}$$

$$\nabla\cdot\boldsymbol{w}_0 = 0 \tag{43}$$

$$\pi_0 \text{ stationary (periodic in periodic geometries)} \tag{44}$$

$$\boldsymbol{w}_0 = 0 \tag{45}$$

In this manner the wanted model parameters (and all next ones if necessary) can in principle be obtained

successively from the microstructure as

$$k_0/\phi \equiv \langle \boldsymbol{w}_0 \rangle \cdot \boldsymbol{e}, \quad \alpha_0 \equiv \frac{\langle \boldsymbol{w}_1 \rangle \cdot \boldsymbol{e}}{(\langle \boldsymbol{w}_0 \rangle \cdot \boldsymbol{e})^2}, \quad \alpha_1^2 \equiv \frac{\langle \boldsymbol{w}_2 \rangle \cdot \boldsymbol{e} \, \langle \boldsymbol{w}_0 \rangle \cdot \boldsymbol{e} - (\langle \boldsymbol{w}_1 \rangle \cdot \boldsymbol{e})^2}{(\langle \boldsymbol{w}_0 \rangle \cdot \boldsymbol{e})^4}, \tag{46}$$

$$\alpha_2^3 \equiv \frac{\langle \boldsymbol{w}_3 \rangle \cdot \boldsymbol{e} \, (\langle \boldsymbol{w}_0 \rangle \cdot \boldsymbol{e})^2 - 2 \langle \boldsymbol{w}_2 \rangle \cdot \boldsymbol{e} \, \langle \boldsymbol{w}_1 \rangle \cdot \boldsymbol{e} \, \langle \boldsymbol{w}_0 \rangle \cdot \boldsymbol{e} + (\langle \boldsymbol{w}_1 \rangle \cdot \boldsymbol{e})^3}{(\langle \boldsymbol{w}_0 \rangle \cdot \boldsymbol{e})^6}. \tag{47}$$

Note that α_0 also writes $\langle \boldsymbol{w}_0 \cdot \boldsymbol{w}_0 \rangle / (\langle \boldsymbol{w}_0 \rangle \cdot \boldsymbol{e})^2$. Indeed, the identity $\langle \boldsymbol{w}_0 \cdot \boldsymbol{w}_0 \rangle = \langle \boldsymbol{w}_1 \rangle \cdot \boldsymbol{e}$ is obtained substituting one times $\boldsymbol{w}_0 = -\Delta \boldsymbol{w}_1 + \nabla \pi_1$, making integrations by parts, using (42), and cancelling some terms using the incompressibility, or the stationary character of the fields and the no-slip boundary condition (see [5, Appendix B]).

In an alternative point of view which can be convenient to use, instead of working with the harmonic regime problem (26-28), we consider the impulse problem [42]

$$\frac{\partial \boldsymbol{v}}{\partial t} = -\nabla (p/\rho_f) + \nu \Delta \boldsymbol{v} + v_0 \boldsymbol{e} \delta(t) \tag{48}$$

$$\nabla \cdot \boldsymbol{v} = 0 \tag{49}$$

$$p/\rho_f \text{ stationary} \tag{50}$$

$$\boldsymbol{v} = \boldsymbol{0} \tag{51}$$

whose solution can be expressed as a sum of normal modes:

$$\frac{\boldsymbol{v}(\boldsymbol{r},t)}{v_0} = \sum_{n=1}^{\infty} b_n e^{-t\nu/\sigma_n} \boldsymbol{\Psi}_n(\boldsymbol{r}), \tag{52}$$

where the eigenfunctions satisfy

$$\Delta \boldsymbol{\Psi}_n - \nabla Q_n = -\sigma_n^{-1} \boldsymbol{\Psi}_n \tag{53}$$

$$\nabla \cdot \boldsymbol{\Psi}_n = 0 \tag{54}$$

$$Q_n \text{ stationary} \tag{55}$$

$$\boldsymbol{\Psi}_n = \boldsymbol{0} \tag{56}$$

Note that the above discrete labelling and summation (as opposed to a continuous and integral one) introduces the assumption that the microgeometry is periodic (or has finite dimensions, such as for cylindrical pores). The inverse eigenvalues σ_n, $n = 1, 2, \ldots$, sorted in descending order, are purely geometrical quantities having dimension of surface. They accumulate in zero with fractal dimension 1/2 when $n \to \infty$ (this is the expression of the asymptotic Johnson et al. [4] high-frequency behavior conditioned by the viscous skin depth parameter $\delta = (2\nu/\omega)^{1/2}$, see [42, Appendix C]) and determine viscous relaxation times through the relation $\Theta_n = \sigma_n/\nu$. The quantities Q_n are fluctuating pressures having no macroscopic gradient, that is, stationary fields (periodic fields in periodic geometries). The eigenfunctions are orthonormal

$$\langle \boldsymbol{\Psi}_m(\boldsymbol{r}) \cdot \boldsymbol{\Psi}_n(\boldsymbol{r}) \rangle = \delta_{mn}, \tag{57}$$

and the eigenfunctions coefficients are

$$b_n = \langle \boldsymbol{\Psi}_n(\boldsymbol{r}) \rangle \cdot \boldsymbol{e}. \tag{58}$$

Noting $\boldsymbol{v}(\boldsymbol{r},s)=\mathcal{L}\left[\boldsymbol{v}(\boldsymbol{r},t)\right]$ the Laplace transform in time, we get, taking the transform of (52)

$$\frac{\boldsymbol{v}(\boldsymbol{r},s)}{v_0}=\sum_{n=1}^{\infty}\frac{b_n}{s+\nu/\sigma_n}\boldsymbol{\Psi}_n(\boldsymbol{r}), \tag{59}$$

and the transform of the problem (48-51)

$$s\boldsymbol{v}=-\nabla\left(p/\rho_f\right)+\nu\Delta\boldsymbol{v}+v_0\boldsymbol{e} \tag{60}$$

$$\nabla\cdot\boldsymbol{v}=0 \tag{61}$$

$$p/\rho_f \text{ stationary} \tag{62}$$

$$\boldsymbol{v}=\boldsymbol{0} \tag{63}$$

which gives by comparison with (29-32) and (33), and by setting $s=\mathrm{j}\omega$, $\boldsymbol{w}=\nu\boldsymbol{v}/v_0$, $\pi=p/\rho_f v_0$,

$$k(\omega)/\phi=\langle\boldsymbol{w}\rangle\cdot\boldsymbol{e}=\sum_{n=1}^{\infty}\frac{b_n}{\frac{\mathrm{j}\omega}{\nu}+\sigma_n^{-1}}\langle\boldsymbol{\Psi}_n(\boldsymbol{r})\rangle\cdot\boldsymbol{e}=\sum_{n=1}^{\infty}\frac{b_n^2}{\frac{\mathrm{j}\omega}{\nu}+\sigma_n^{-1}} \tag{64}$$

This distribution of relaxation times representation explicitly shows that for ω below the convergence radius $\omega_c=\nu\sigma_1^{-1}$ the dynamic permeability expands in a power series of $-\mathrm{j}\omega/\nu$:

$$k(\omega)/\phi=\sum_{n=1}^{\infty}\frac{b_n^2\sigma_n}{1-\left(-\frac{\mathrm{j}\omega}{\nu}\sigma_n\right)}=\sum_{n=1}^{\infty}b_n^2\sigma_n\left[1+\left(-\frac{\mathrm{j}\omega}{\nu}\sigma_n\right)+\left(-\frac{\mathrm{j}\omega}{\nu}\sigma_n\right)^2+\ldots\right]. \tag{65}$$

Writing by definition

$$k(\omega)/\phi=S_1+\left(\frac{-\mathrm{j}\omega}{\nu}\right)S_2+\ldots+\left(\frac{-\mathrm{j}\omega}{\nu}\right)^m S_{m+1}+\ldots, \tag{66}$$

the comparison with (36) and (65) gives

$$S_m=\langle\boldsymbol{w}_{m-1}\rangle\cdot\boldsymbol{e}=\sum_{n=1}^{\infty}b_n^2\sigma_n^m. \tag{67}$$

Recall that in (37) we defined the characteristic viscous angular frequency

$$\omega_v=\frac{\nu}{\langle\boldsymbol{w}_0\rangle\cdot\boldsymbol{e}}=\frac{\nu\phi}{k_0}\equiv\frac{\nu}{S_1}.$$

The above "distribution of relaxation times" representation, joined to the relation (33), now allows us to conclude that the dynamic tortuosity has the following Laurent-series expansion, of convergence radius $\omega_c=\nu\sigma_1^{-1}$, starting with power -1:

$$\alpha(\omega)=\frac{\omega_v}{\mathrm{j}\omega}+\alpha_0+\alpha_1^2\left(\frac{-\mathrm{j}\omega}{\omega_v}\right)+\alpha_2^3\left(\frac{-\mathrm{j}\omega}{\omega_v}\right)^2+\alpha_3^4\left(\frac{-\mathrm{j}\omega}{\omega_v}\right)^3+\alpha_4^5\left(\frac{-\mathrm{j}\omega}{\omega_v}\right)^4+\ldots \tag{68}$$

and with alpha coefficients α_p^{p+1} (dimensionless form-factors) given in terms of the S_m as follows, after

straightforward calculations:

$$\alpha_0 = \frac{S_2}{S_1^2}, \quad \alpha_1^2 = \frac{S_3 S_1 - S_2^2}{S_1^4}, \quad \alpha_2^3 = \frac{S_4 S_1^2 - 2S_3 S_2 S_1 + S_2^3}{S_1^6}, \quad \alpha_3^4 = \frac{S_5 S_1^3 - 2S_4 S_2 S_1^2 - S_3^2 S_1^2 + 3S_3 S_2^2 S_1 - S_2^4}{S_1^8}, \tag{69}$$

$$\alpha_4^5 = \frac{S_6 S_1^4 - 2S_5 S_2 S_1^3 - 2S_4 S_3 S_1^3 + 3S_4 S_2^2 S_1^2 + 3S_3^2 S_2 S_1^2 - 4S_3 S_2^3 S_1 + S_2^5}{S_1^{10}}. \tag{70}$$

This formulation leads to easy evaluations of the α_p for the case of cylindrical circular pores of radius a. Following [42, Appendix B], we have $b_n^2 = 4\sigma_n/a^2$, $\sigma_n = a^2/z_n^2$, where z_n, $n = 1, 2, 3, \ldots$ are the zeros of the Bessel function J_0. This gives

$$S_m = a^{2m} \sum_{n=1}^{+\infty} \frac{4}{z_n^{2(1+m)}} \tag{71}$$

which can be readily evaluated. In this manner we find the following reference values for the first successive α_p in cylindrical circular pores:

$$\begin{aligned} &\alpha_0 = 1.333333 \\ &\alpha_1^2 = 0.0555555 \rightarrow \alpha_1 = 0.235702 \\ &\alpha_2^3 = 0.0148148 \rightarrow \alpha_2 = 0.245602 \\ &\alpha_3^4 = 0.0043209 \rightarrow \alpha_3 = 0.256387 \\ &\alpha_4^5 = 0.0012933 \rightarrow \alpha_4 = 0.264450 \end{aligned} \tag{72}$$

The successive α_p, $p = 1, 2, 3, \ldots$ are pretty close, which reflects the absence of different pores sizes, however they have a trend to steadily increase. This increase can be interpreted in terms of the fact anticipated in Section C, that, because the convergence radius ω_c is finite, the addition of monomials in the series must accelerate as the frequency increases, or in other words, the corrections made by successive monomials remain significant in themselves only for smaller and smaller frequency increases as the frequency goes closer to ω_c.

B Determination of the transmission operator

The direct scattering problem requires finding the pressure field transmitted by the porous material. Let us consider here a rigid-frame, air-filled isotropic porous medium inside a finite region $0 \leq x \leq L$, as depicted in Fig. 15. We consider the general case where a sound pulse impinges on the medium from the left with an incident angle θ^i. To derive the required operator, continuity of pressure and velocity on the two interfaces of the material is assumed, resulting in the interface conditions [43]

$$\begin{cases} p(0^-, t) = p(0^+, t), \quad p(L^-, t) = p(L^+, t) \\ v(0^-, t) = \phi v(0^+, t), \quad \phi v(L^-, t) = v(L^+, t) \end{cases} \tag{73}$$

where a porosity of 1 has been taken for the ambient fluid ($x < 0$, $x > L$), and where the $-$ superscript stands for the left side of an interface, and the $+$ superscript stands for its right side. We note $P(\boldsymbol{x}, \omega)$ (resp. $V(\boldsymbol{x}, \omega)$) the Fourier transform of $p(\boldsymbol{x}, t)$ (resp. $v(\boldsymbol{x}, t)$) defined by

$$P(\boldsymbol{x}, \omega) = \mathcal{F}\left[p(\boldsymbol{x}, t)\right] = \int_{-\infty}^{\infty} \exp\left(-\mathrm{j}\omega t\right) p(\boldsymbol{x}, t) \mathrm{d}t, \tag{74}$$

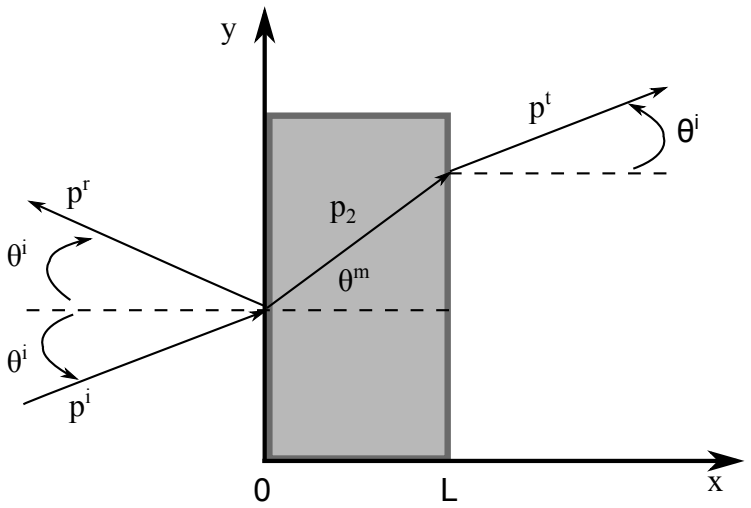

Figure 15: Schematic of the scattering problem

and the inverse Fourier transform by $p(\boldsymbol{x},t) = \mathcal{F}^{-1}\left[P(\boldsymbol{x},\omega)\right]$. The expression of the pressure field in the region on the left side of the material is the sum of the incident and reflected fields

$$p_1(\boldsymbol{x},t) = p^i\left(t - \frac{x}{c_f}\cos\theta^i - \frac{y}{c_f}\sin\theta^i\right) + p^r\left(t + \frac{x}{c_f}\cos\theta^i - \frac{y}{c_f}\sin\theta^i\right), \tag{75}$$

where $c_f = \sqrt{K_f/\rho_f} \approx 340\,\mathrm{m.s^{-1}}$ is the sound speed in air. In the Fourier domain, the fields on the left side of the material become, for $x < 0$ [44]

$$\begin{cases} P_1(\boldsymbol{x},\omega) = & \left(e^{-\mathrm{j}\omega\frac{x}{c_f}\cos\theta^i} + R(\omega,\theta^i)e^{\mathrm{j}\omega\frac{x}{c_f}\cos\theta^i}\right)e^{-\mathrm{j}\omega\frac{y}{c_f}\sin\theta^i} \\ V_1(\boldsymbol{x},\omega) = & \frac{\cos\theta^i}{Z_f}\left(e^{-\mathrm{j}\omega\frac{x}{c_f}\cos\theta^i} - R(\omega,\theta^i)e^{\mathrm{j}\omega\frac{x}{c_f}\cos\theta^i}\right)e^{-\mathrm{j}\omega\frac{y}{c_f}\sin\theta^i} \end{cases} \tag{76}$$

where $R(\omega,\theta^i)$ is the Fourier transform of a reflection kernel, $Z_f = \rho_f c_f \approx 418\,\mathrm{kg.m^{-2}.s^{-1}}$ is the characteristic impedance of the material, and $V_1(\boldsymbol{x},\omega)$ is the x component of the velocity. Inside the material, the fields are expressed, for $0 \leq x \leq L$, as

$$\begin{cases} P_2(\boldsymbol{x},\omega) = & \left(A(\omega)e^{-\mathrm{j}\omega\frac{x}{c_m}\cos\theta^m} + B(\omega)e^{\mathrm{j}\omega\frac{x}{c_m}\cos\theta^m}\right)e^{-\mathrm{j}\omega\frac{y}{c_m}\sin\theta^m} \\ V_2(\boldsymbol{x},\omega) = & \frac{\cos\theta_1}{Z_m}\left(A(\omega)e^{-\mathrm{j}\omega\frac{x}{c_m}\cos\theta^m} - B(\omega)e^{\mathrm{j}\omega\frac{x}{c_m}\cos\theta^m}\right)e^{-\mathrm{j}\omega\frac{y}{c_m}\sin\theta^m} \end{cases} \tag{77}$$

where $A(\omega)$ and $B(\omega)$ are unknown parameters (the angle dependency is omitted for clarity), θ^m is the refracted wave angle in the porous material, relative to its normal, and $V_2(\boldsymbol{x},\omega)$ is the x component of the velocity. The phase velocity in the equivalent fluid material is defined as $c_m = c_f/\sqrt{\alpha(\omega)\beta(\omega)}$, while the characteristic impedance of the material is given by $Z_m = Z_f\sqrt{\frac{\alpha(\omega)}{\beta(\omega)}}$. Finally, on the right side of the material, the transmitted fields are expressed, for $L \leq x < +\infty$, as

$$\begin{cases} P_3(\boldsymbol{x},\omega) = & T(\omega,\theta^i)e^{-\mathrm{j}\omega\frac{x-L}{c_f}\cos\theta^i}e^{-\mathrm{j}\omega\frac{y}{c_f}\sin\theta^i} \\ V_3(\boldsymbol{x},\omega) = & \frac{\cos\theta^i}{Z_f}T(\omega,\theta^i)e^{-\mathrm{j}\omega\frac{x-L}{c_f}\cos\theta^i}e^{-\mathrm{j}\omega\frac{y}{c_f}\sin\theta^i} \end{cases} \tag{78}$$

where $T(\omega,\theta^i)$ is the Fourier transform of the transmission kernel.
Using the boundary conditions of Eq. 73, one obtains the set of 4 equations and 4 unknowns

$$\begin{cases} 1 + R(\omega, \theta^i) = A(\omega) + B(\omega) \\ T(\omega, \theta^i) = A(\omega) e^{-\mathrm{j}\omega \frac{L}{c_m} \cos\theta^m} + B(\omega) e^{\mathrm{j}\omega \frac{L}{c_m} \cos\theta^m} \\ 1 - T(\omega, \theta^i) = \phi \frac{Z_f \cos\theta^m}{Z_m \cos\theta^i} \left(A(\omega) - B(\omega)\right) \\ T(\omega, \theta^i) = \phi \frac{Z_f \cos\theta^m}{Z_m \cos\theta^i} \left(A(\omega) e^{-\mathrm{j}\omega \frac{L}{c_m} \cos\theta^m} - B(\omega) e^{\mathrm{j}\omega \frac{L}{c_m} \cos\theta^m}\right) \end{cases} \tag{79}$$

Solving the system 79 yields the reflection coefficient $R(\omega, \theta^i)$ and transmission coefficient $T(\omega, \theta^i)$, as

$$R(\omega, \theta^i) = \frac{(1 - \Xi^2)}{(1 + \Xi^2) + 2\Xi \coth(\mathrm{j}\omega L \xi_m)}, \quad T(\omega, \theta^i) = \frac{2\Xi}{2\Xi \cosh(\mathrm{j}\omega L \xi_m) + (1 + \Xi)^2 \sinh(\mathrm{j}\omega L \xi_m)}, \tag{80}$$

with

$$\Xi = \phi \sqrt{\frac{\beta(\omega)}{\alpha(\omega)}}, \quad \xi_m = \sqrt{\frac{\rho_f}{K_f} \alpha(\omega)\beta(\omega)}, \quad \cos\theta^m = \sqrt{1 - \frac{\sin^2\theta^i}{\alpha(\omega)\beta(\omega)}}. \tag{81}$$

A particular relation that was used is the Snell-Descartes law of refraction, relating the angles of refraction in the two domains to the speed of sound as

$$\frac{\sin\theta^i}{c_f} = \frac{\sin\theta^m}{c_m}, \tag{82}$$

which yields

$$\sin\theta^m = \frac{\sin\theta^i}{\sqrt{\alpha(\omega)\beta(\omega)}}, \tag{83}$$

and thus,

$$\cos\theta^m = \sqrt{1 - \sin^2\theta^m} = \sqrt{1 - \frac{\sin^2\theta^i}{\alpha(\omega)\beta(\omega)}}. \tag{84}$$

The expression in Eq. 14 is then obtained by setting $\theta^i = 0$ in Eqs. 80,81.

References

[1] J. Allard, N. Atalla, Propagation of Sound in Porous Media: Modelling Sound Absorbing Materials 2e, John Wiley & Sons, 2009. doi:10.1002/9780470747339.

[2] J. Bear, Dynamics of fluids in porous media, Courier Corporation, 2013.

[3] K. Vafai, Porous media: applications in biological systems and biotechnology, CRC Press, 2010.

[4] D. L. Johnson, J. Koplik, R. Dashen, Theory of dynamic permeability and tortuosity in fluid-saturated porous media, J. Fluid Mech. 176 (1987) 379–402. doi:10.1017/S0022112087000727.

[5] A. Norris, On the viscodynamic operator in biot's equations of poroelasticity, J. Wave Mat. Interact 1 (1986) 365–380.

[6] D. Lafarge, Propagation du son dans les matériaux poreux à structure rigide saturés par un fluide viscothermique: Définition de paramètres géométriques, analogie electromagnétique, temps de relaxation, Ph.D. thesis (1993).
URL http://cyberdoc.univ-lemans.fr/theses/1993/1993LEMA1009.pdf

[7] D. Lafarge, P. Lemarinier, J. F. Allard, V. Tarnow, Dynamic compressibility of air in porous structures at audible frequencies, J. Acoust. Soc. Am. 102 (4) (1997) 1995–2006. doi:10.1121/1.419690.

[8] L. L. Beranek, Acoustical properties of homogeneous, isotropic rigid tiles and flexible blankets, J. Acoust. Soc. Am. 19 (4) (1947) 556–568.

[9] R. L. Brown, R. H. Bolt, The measurement of flow resistance of porous acoustic materials, J. Acoust. Soc. Am. 13 (4) (1942) 337–344. doi:http://dx.doi.org/10.1121/1.1916184.

[10] Z. E. A. Fellah, S. Berger, W. Lauriks, C. Depollier, C. Aristegui, J.-Y. Chapelon, Measuring the porosity and the tortuosity of porous materials via reflected waves at oblique incidence, J. Acoust. Soc. Am. 113 (5) (2003) 2424–2433. doi:10.1121/1.1567275.

[11] P. Leclaire, L. Kelders, W. Lauriks, M. Melon, N. Brown, B. Castagnede, Determination of the viscous and thermal characteristic lengths of plastic foams by ultrasonic measurements in helium and air, J. App. Phys. 80 (4) (1996) 2009–2012. doi:10.1063/1.363817.

[12] K. V. Horoshenkov, A review of acoustical methods for porous material characterisation, Int. J. Acoust. Vib 22 (2017) 92–103.

[13] K. Attenborough, I. Bashir, S. Taherzadeh, Outdoor ground impedance models, The Journal of the Acoustical Society of America 129 (5) (2011) 2806–2819. doi:10.1121/1.3569740.

[14] Z. E. A. Fellah, M. Fellah, N. Sebaa, W. Lauriks, C. Depollier, Measuring flow resistivity of porous materials at low frequencies range via acoustic transmitted waves, The Journal of the Acoustical Society of America 119 (4) (2006) 1926–1928.

[15] A. Berbiche, M. Sadouki, Z. Fellah, E. Ogam, M. Fellah, F. Mitri, C. Depollier, Experimental determination of the viscous flow permeability of porous materials by measuring reflected low frequency acoustic waves, Journal of Applied Physics 119 (1) (2016) 014906.

[16] Z. E. A. Fellah, M. Fellah, F. Mitri, N. Sebaa, W. Lauriks, C. Dépollier, Transient acoustic wave propagation in air-saturated porous media at low frequencies, Journal of Applied physics 102 (8) (2007) 084906.

[17] M. Sadouki, M. Fellah, Z. E. A. Fellah, E. Ogam, N. Sebaa, F. Mitri, C. Depollier, Measuring static thermal permeability and inertial factor of rigid porous materials (l), J. Acoust. Soc. Am. 130 (5) (2011) 2627–2630.

[18] T. G. Zieliński, Normalized inverse characterization of sound absorbing rigid porous media, J. Acoust. Soc. Am. 137 (6) (2015) 3232–3243. doi:10.1121/1.4919806.

[19] Y. Champoux, J.-F. Allard, Dynamic tortuosity and bulk modulus in air-saturated porous media, J. Appl. Acoust. 70 (4) (1991) 1975–1979. doi:10.1063/1.349482.

[20] J.-D. Chazot, E. Zhang, J. Antoni, Acoustical and mechanical characterization of poroelastic materials using a bayesian approach, J. Acoust. Soc. Am. 131 (6) (2012) 4584–4595. doi:10.1121/1.3699236.

[21] M. Niskanen, J.-P. Groby, A. Duclos, O. Dazel, J. Le Roux, N. Poulain, T. Huttunen, T. Lähivaara, Deterministic and statistical characterization of rigid frame porous materials from impedance tube measurements, J. Acoust. Soc. Am. 142 (4) (2017) 2407–2418. doi:10.1121/1.5008742.

[22] R. Roncen, Z. Fellah, F. Simon, E. Piot, M. Fellah, E. Ogam, C. Depollier, Bayesian inference for the ultrasonic characterization of rigid porous materials using reflected waves by the first interface, The Journal of the Acoustical Society of America 144 (1) (2018) 210–221.

[23] J. Kergomard, D. Lafarge, J. Gilbert, Transients in porous media: exact and modelled time-domain green's functions, Acta Acustica united with Acustica 99 (4) (2013) 557–571.

[24] M. A. Biot, Theory of propagation of elastic waves in a fluid-saturated porous solid. i. low-frequency range, J. Acoust. Soc. Am. 28 (2) (1956) 168–178. doi:10.1121/1.1908239.

[25] C. Zwikker, C. W. Kosten, Sound absorbing materials, Elsevier, 1949.

[26] Z. Fellah, C. Depollier, Transient acoustic wave propagation in rigid porous media: A time-domain approach, The Journal of the Acoustical Society of America 107 (2) (2000) 683–688.

[27] C.-Y. Lee, M. J. Leamy, J. H. Nadler, Frequency band structure and absorption predictions for multi-periodic acoustic composites, Journal of Sound and Vibration 329 (10) (2010) 1809–1822.

[28] C. Boutin, C. Geindreau, Estimates and bounds of dynamic permeability of granular media, The Journal of the Acoustical Society of America 124 (6) (2008) 3576–3593.

[29] R. J. Brown, Connection between formation factor for electrical resistivity and fluid-solid coupling factor in biot's equations for acoustic waves in fluid-filled porous media, Geophysics 45 (8) (1980) 1269–1275.

[30] D. Smeulders, R. Eggels, M. Van Dongen, Dynamic permeability: reformulation of theory and new experimental and numerical data, Journal of Fluid Mechanics 245 (1992) 211–227. doi:10.1017/S0022112092000429.

[31] R. C. Smith, Uncertainty quantification: theory, implementation, and applications, Vol. 12, Siam, 2013.

[32] A. Tarantola, Inverse problem theory and methods for model parameter estimation, SIAM, 2005. doi:10.1137/1.9780898717921.bm.

[33] J. Kaipio, E. Somersalo, Statistical and computational inverse problems, Vol. 160, Springer Science & Business Media, 2006.

[34] S. Torquato, Relationship between permeability and diffusion-controlled trapping constant of porous media, Physical review letters 64 (22) (1990) 2644.

[35] N. Metropolis, A. W. Rosenbluth, M. N. Rosenbluth, A. H. Teller, E. Teller, Equation of state calculations by fast computing machines, The journal of chemical physics 21 (6) (1953) 1087–1092. doi:10.1063/1.1699114.

[36] W. K. Hastings, Monte carlo sampling methods using markov chains and their applications, Biometrika 57 (1) (1970) 97–109.

[37] W. R. Gilks, S. Richardson, D. Spiegelhalter, Markov chain Monte Carlo in practice, CRC press, 1995.

[38] E. Laloy, J. A. Vrugt, High-dimensional posterior exploration of hydrologic models using multiple-try dream(zs) and high-performance computing, Water Resour. Res. 48 (1) (2012) n/a–n/a, w01526. doi:10.1029/2011WR010608.

[39] A. Gelman, D. B. Rubin, Inference from iterative simulation using multiple sequences, Statistical science 7 (4) (1992) 457–472.
URL http://www.jstor.org/stable/2246093

[40] Y. Champoux, M. R. Stinson, G. A. Daigle, Air-based system for the measurement of porosity, J. Acoust. Soc. Am. 89 (2) (1991) 910–916. doi:10.1121/1.1894653.

[41] D. Bies, C. H. Hansen, Flow resistance information for acoustical design, Applied Acoustics 13 (5) (1980) 357–391.

[42] M. Avellaneda, S. Torquato, Rigorous link between fluid permeability, electrical conductivity, and relaxation times for transport in porous media, Physics of Fluids A: Fluid Dynamics 3 (11) (1991) 2529–2540.

[43] B. Gurevich, M. Schoenberg, Interface conditions for biot's equations of poroelasticity, The Journal of the Acoustical Society of America 105 (5) (1999) 2585–2589.

[44] Z. E. A. Fellah, M. Fellah, W. Lauriks, C. Depollier, Direct and inverse scattering of transient acoustic waves by a slab of rigid porous material, J. Acoust. Soc. Am. 113 (1) (2003) 61–72. doi:10.1121/1.1528592.